Applied Geochemistry 206 (2026) 106914

Contents lists available at ScienceDirect

Applied Geochemistry

journal homepage: www.elsevier.com/locate/apgeochem

Tracing nutrient uplift from permafrost thaw using radiogenic Sr isotopes in plants: A field-based soil warming experiment

Philippe Roux [a,*], Damien Lemarchand [b], Edward A.G. Schuur [c], Sophie Opfergelt [a]

[a] Earth and Life Institute, Université Catholique de Louvain, Louvain-la-Neuve, Belgium
[b] Institut Terre et Environnement Strasbourg (ITES), Université de Strasbourg-EOST, CNRS, ENGEES, Strasbourg, France
[c] Center for Ecosystem Science and Society, Northern Arizona University, Flagstaff, AZ, USA

ARTICLE INFO

Editorial handling by: Wenfeng Tan

ABSTRACT

Permafrost thaw in Arctic ecosystems is altering soil structure and hydrology, deepening the active layer and increasing the availability of nutrients previously locked in frozen ground. These changes contribute to the current trend of increased plant productivity and shifts in species composition. Because arctic plant functional types have specific nutrient acquisition strategies due to differing rooting depths, it is therefore essential to identify the mechanisms responsible for changes in nutrient sources during permafrost degradation. The aim of this study is to quantify the contribution of biological cycling and/or water table rise to nutrient sources available to four major plants upon permafrost thaw. To do so, we developed a mass balance model based on an eight-year soil warming experiment on the Eight Mile Lake study site in Interior Alaska. This model combines vegetation composition survey, water table depth data with foliar strontium (Sr) concentrations and isotopic composition ($^{87}Sr/^{86}Sr$) to simulate Sr transfer in the soil-plant system. Our results show that biocycling alone is sufficient to explain the isotopic shift under control conditions for all four plants. Under soil warming, however, biocycling accounts for 37-54% of the observed shift for shallow and intermediate rooted species, while water table rise accounts for 35-47%. Although all modelled values remain within the range of observed variability, 2-20% of the observed shift remains unresolved across species. While permafrost thaw is a key source of newly available nutrients, our model suggests that redistribution mechanisms are the primary drivers of changes in plant nutrient sources.

1. Introduction

Arctic and sub-Arctic ecosystems are underlain by permafrost, a layer of permanently frozen soil or rock for at least two consecutive years (French, 2007). The active layer, the section of soil above the permafrost that thaws seasonally, constrains biological activity and, consequently, vegetation growth due to a short growing season, low soil temperatures and restricted rooting depth (Mauclet et al., 2022). However, global temperature increase is accelerating permafrost degradation, leading to active layer deepening and therefore increasing the volume of soil accessible to plants. This will modify nutrient dynamics and thereby influencing the mobility of mineral elements and soil–plant nutrient cycling (Hewitt et al., 2019; Hirst et al., 2022; Jorgenson et al., 2006; Koch et al., 2013; Mauclet et al., 2022, 2023; Salmon et al., 2016; Schuur and Mack, 2018; Villani et al., 2022; Walvoord and Kurylyk, 2016). These changes have driven a significant increase in vegetation productivity since the early 1980s, a phenomenon called Arctic greening (Elmendorf et al., 2012; Frost et al., 2020; Heijmans et al., 2022; Myers-Smith et al., 2020). This trend causes significant feedback to climate dynamics by altering surface energy balance (ground albedo, solar radiation, and shading) (Heijmans et al., 2022; Sturm et al., 2001). It can also modify ecosystem carbon balance through respiration, photosynthesis, litter and soil organic matter degradation (Cornelissen et al., 2007; Natali et al., 2012; Schuur et al., 2007, 2021; Shaver et al., 2006).

The increase vegetation productivity that characterizes Arctic greening is primarily driven by warmer, longer growing seasons (Blume-Werry, 2021; Euskirchen et al., 2006; Heijmans et al., 2022), increased precipitation (Heijmans et al., 2022; McCrystall et al., 2021; Van Der Kolk et al., 2016), atmospheric CO_2 concentrations (Heijmans et al., 2022; Mcguire et al., 2009; Myers-Smith et al., 2015), as well as enhanced access to nutrients released from permafrost thaw

* Corresponding author.
E-mail address: philippe.roux@observatory.be (P. Roux).

https://doi.org/10.1016/j.apgeochem.2026.106914
Received 28 September 2025; Received in revised form 30 April 2026; Accepted 27 May 2026
Available online 28 May 2026

(Blume-Werry et al., 2019; Heijmans et al., 2022; Hewitt et al., 2019; Keuper et al., 2012; Salmon et al., 2016; Van Der Kolk et al., 2016; Wang et al., 2017). These environmental changes affect the distribution patterns of tundra plant functional types with two distinct shifts occurring over the past decades: an increase in shrub dominance in well-drained areas (Jónsdóttir et al., 2005; Schuur et al., 2007; Shaver et al., 2001; Sturm et al., 2001), and an expansion of graminoid in subsided, poorly drained zones where permafrost thaw has altered soil hydrology (Jorgenson et al., 2001, 2015; Osterkamp et al., 2009; Van Der Kolk et al., 2016). The biomass distribution of these plant functional types is therefore largely shaped by active layer depth and water table fluctuations across permafrost environment (Heijmans et al., 2022). Nevertheless, newly available nutrients from permafrost thaw are also expected to contribute to higher vegetation productivity and ongoing shifts in Arctic plant communities (Chapin et al., 1995; Keuper et al., 2017; Nadelhoffer et al., 1991; Schuur et al., 2007; Van Der Kolk et al., 2016). The ability of plants to effectively take advantage of these newly available nutrients ultimately depends on their nutrient acquisition strategies as different functional groups are characterized by different rooting depths and, consequently, access to different nutrient sources (Iversen et al., 2015). For instance, the maximum rooting depth of *Eriophorum vaginatum* allows it to access thawed permafrost nutrients because of their deep rooting system, while species like *Betula nana* and *Vaccinium vitis-idaea* are shallow-rooted and therefore rely more on upper soil layers and nutrient pulses following snowmelt (Blume-Werry et al., 2019; Hewitt et al., 2019; Salmon et al., 2016; Wang et al., 2017). This vertical stratification of rooting depth across different plant functional types suggests that nutrient released by permafrost thaw would only benefit deep-rooted species. However, recent observations at a thawing site in Interior Alaska have shown foliar nutrients to originate from deeper mineral soil horizons across plants of all rooting depths (Mauclet et al., 2023a,b). Because the deepening of root distributions induced by warming appears to be mostly limited to deep-rooted sedges (Blume-Werry et al., 2019; Wang et al., 2017), this shift in nutrient sources cannot be explained by root plasticity alone. Instead, vertical redistribution processes are required to make mineral elements released from thawed soil layers available to shallow-rooted plants. Identifying the mechanisms driving this redistribution is therefore essential to predict and understand how Arctic plant communities will respond to permafrost thaw (Van Der Kolk et al., 2016).

Two major processes may contribute to nutrient redistribution in Arctic soils upon warming: biocycling and water table rise. Biocycling refers to the plant-mediated loop through which nutrients taken up at depth by roots are returned to the surface organic layer: root uptake from distinct soil layers, incorporation into plant biomass, transfer to the litter layer through leaf senescence mineralization of litter back into the upper soil (Jobbágy and Jackson, 2004). The increase in biomass productivity and litter decomposition induced by climate change can therefore gradually accelerate nutrient turnover over years or decades, thus shaping soil nutrient dynamics over time (McLaren et al., 2017). In parallel, water table fluctuations caused by permafrost thaw can result in the more rapid transfer of deeper soil nutrients to shallower soil layers within seasons to years, as demonstrated for iron by previous studies (Herndon et al., 2020; Monhonval et al., 2023). Quantifying the relative contributions of these processes is therefore essential for predicting Arctic ecosystem trajectories and improving climate models that rely on nutrient-vegetation feedback, as they operate on different timescales and respond to distinct environmental drivers.

In this context, the $^{87}Sr/^{86}Sr$ ratio has been largely used to trace cation sources at the Earth surface using bedrock composition and mineral weathering dynamics (Drouet et al., 2005, 2007; Wang and Tang, 2020). Strontium is a geochemical analogue of calcium as both are divalent alkaline cations with similar ionic radii, allowing it to follow the same uptake pathways in the soil plant system (Capo et al., 1998; White, 2001). Plants take up Sr primarily from the soil exchangeable fraction and $^{87}Sr/^{86}Sr$ ratios in plant tissues are expected to reflect the weighted average isotopic composition of the exchangeable Sr sources supplying uptake, rather than bulk mineral Sr (Chadwick et al., 1999; Drouet et al., 2005). Sr passively enters plants through non-selective pathways, with little evidence for physiological discrimination with Ca (Capo et al., 1998; White, 2001) or $^{87}Sr/^{86}Sr$ (Chadwick et al., 1999; Drouet et al., 2005; Reynolds et al., 2012), thus making it a conservative tracer of plant cation sources (Chadwick et al., 1999; Drouet et al., 2005, 2007; Mauclet et al., 2023a,b; Vitousek et al., 1999). Chadwick et al. (1999) demonstrated this principle across the Hawaiian Islands chronosequence, where $^{87}Sr/^{86}Sr$ ratios in *Metrosideros* leaves closely tracked those of the soil exchangeable fraction as ecosystems transitioned from rock-derived to atmospherically derived cation sources. (Chadwick et al., 1999; Mauclet et al., 2023; Reynolds et al., 2012; Vitousek et al., 1999). At the Eight Mile Lake study site, Mauclet et al. (2023a,b) revealed a systematic decrease in exchangeable $^{87}Sr/^{86}Sr$ ratios with soil depth, reflecting the transition from weathered clay minerals in organic horizons to less radiogenic primary minerals in mineral horizons. Importantly, they found that foliar $^{87}Sr/^{86}Sr$ ratios decreased from *Vaccinium vitis-idaea* to *Betula nana* to *Eriophorum vaginatum*, reflecting their respective rooting depths. All three plant functional types showed lower foliar $^{87}Sr/^{86}Sr$ ratios in highly thawed compared to poorly thawed soil profiles. This shift indicated that shallow-rooted shrubs also accessed nutrients from deeper, less radiogenic sources upon permafrost thaw. This finding challenges the conventional view that permafrost thaw primarily benefits deep-rooted species. However, the mechanisms driving this shift, whether through accelerated biological recycling or water table rise, remained unclear.

The aim of this study is to quantify the contribution of biological cycling and/or water table rise to nutrient sources available to vegetation upon permafrost thaw. Based on an eight-year soil warming experiment (Eight Mile Lake, Alaska, USA), we measured the foliar Sr concentrations and $^{87}Sr/^{86}Sr$ of four typical tundra plants with contrasted rooting depth collected before (2009) and after (2017) the warming experiment. By combining vegetation composition survey and water table depth data with foliar Sr concentrations and $^{87}Sr/^{86}Sr$ ratio, we apply mass balance equations to quantify the relative contributions of biocycling and water table rise to plant nutrient sources.

2. Materials and methods

2.1. Site description

Established in 2008, the Carbon in Permafrost Experimental Heating Research (CiPEHR) project is located in the Eight Mile Lake Watershed, in the northern foothills of the Alaska Range (63.88°N, −149.23°W, 670 m). This site is characterized by moist, acidic tundra underlain by degrading permafrost within the discontinuous permafrost zone (Natali et al., 2011; Osterkamp et al., 2009). Soils are classified as Cryosols (WRB soil classification) characterized by a thick organic layer (25 to 35 cm) with over 20% organic carbon overlying cryoturbated mineral soil with less than 20% organic carbon, composed of a mixture of glacial till (small stones and cobbles) and windblown loess (Osterkamp et al., 2009; Pries et al., 2012; Vogel et al., 2009). Local air temperatures range from −16 °C in December to +15 °C in July with a mean annual temperature of −0.9 °C. Local average annual precipitation reaches 381 mm. Active layer depth reached approximately 50 cm at the beginning of the experiment. Vegetation at the site is dominated by the tussock-forming sedge *Eriophorum vaginatum* with the only other sedge species being *Carex bigelowii*. Other common vascular plants include *Betula nana* and *Vaccinium uliginosum* from the deciduous shrub functional group; the forb *Rubus chamaemorus;* and evergeen species *Rhododendron tomentosum*, *Oxycoccus microcarpus, Vaccinium vitis-idaea, Empetrum nigrum* and *Andromeda polifolia*. Nonvascular plants are primarily composed of feather mosses, including *Sphagnum* species, and lichens, mostly from the genus *Cladonia* (Deane-Coe et al., 2015; Natali et al., 2012; Schuur et al., 2007).

2.2. Experimental design

The CiPEHR experiment investigated how artificially elevated temperatures influence permafrost thaw and ecosystem carbon dynamics. Our study focuses on two of the four treatments used in the original experimental design: the control plots without warming and plots receiving soil warming treatment. For this treatment, snow fences were used to create snowpacks on their leeward sides which insulated the soil throughout winter. Excess snow was removed in early spring to maintain consistent snowmelt timing across treatments, isolating the thermal effects of increased snow cover from changes in moisture availability. A detailed description of the experimental setup can be found in Natali et al. (2011). Water wells installed at each fence in May 2009 allowed measurements of water table depth (WTD) relative to the soil surface to be measured three times per week during the thaw season. The wells reached depths of 0.6 to 1.0 m below the surface into both soil layers and permafrost (Warren et al., 2025). Thaw depth was measured weekly using a metal probe.

Since the start of the experiment, the soil warming treatment has amplified active layer deepening by up to 6 cm yr^{-1} compared to 2 cm yr^{-1} in the control (Mauritz et al., 2017). Soil subsidence processes between 2009 and 2017 resulted in shallower water tables, thus leading to wetter soil conditions (Supplementary Figs. 1 and 2, adapted from Rodenhizer et al., 2020; Schuur et al., 2023). Vegetation also underwent significant changes, with total foliar biomass increasing by 30% and 26 % in the control and soil warming treatment, respectively (Fig. 1, based on data from Kadej et al., 2022). The sedge species *Eriophorum vaginatum* showed the highest increase in biomass productivity, with relative abundance increasing from 85% in the control (140% absolute biomass) to 125% under soil warming (183% absolute biomass). The total biomass productivity gains between 2009 and 2017 were primarily driven by this increase (Salmon et al., 2016) while lichen and moss species showed significant decline, with their relative abundance decreasing up to 70% in the soil warming treatment. Evergreen biomass remained constant overall, with slight changes in abundance of individual species such as *Rhododendron tomentosum* (13-29% increase) and *Vaccinium vitis-idaea* (32-70% decrease).

This study focuses on four of the most abundant vascular species, representing three functional groups: *Eriophorum vaginatum* (sedge), *Betula nana* and *Vaccinium uliginosum* (deciduous shrub), and *Vaccinium vitis-idaea* (evergreen shrub). Together, these species accounted for 62–66% of total vascular plant foliar biomass in 2009, increasing to 75% by 2017. Additionally, the rooting depth of these plants shows a gradual increase from evergreen shrubs to deciduous shrubs to sedges (Iversen et al., 2015).

2.3. Foliar sampling method

During the peak growing seasons of 2009 and 2017, fully expanded current-year leaves (including petioles) were collected (Natali et al., 2011). Leaves from multiple individuals were sampled over an area of approximately 1 m^2 to account for intraspecies variability before being pooled into a single bulk foliar sample per plot. This procedure was carried out for the four selected plant species across 24 treated plots, resulting in 175 total foliar samples: 95 from control plots and 80 from soil warming plots.

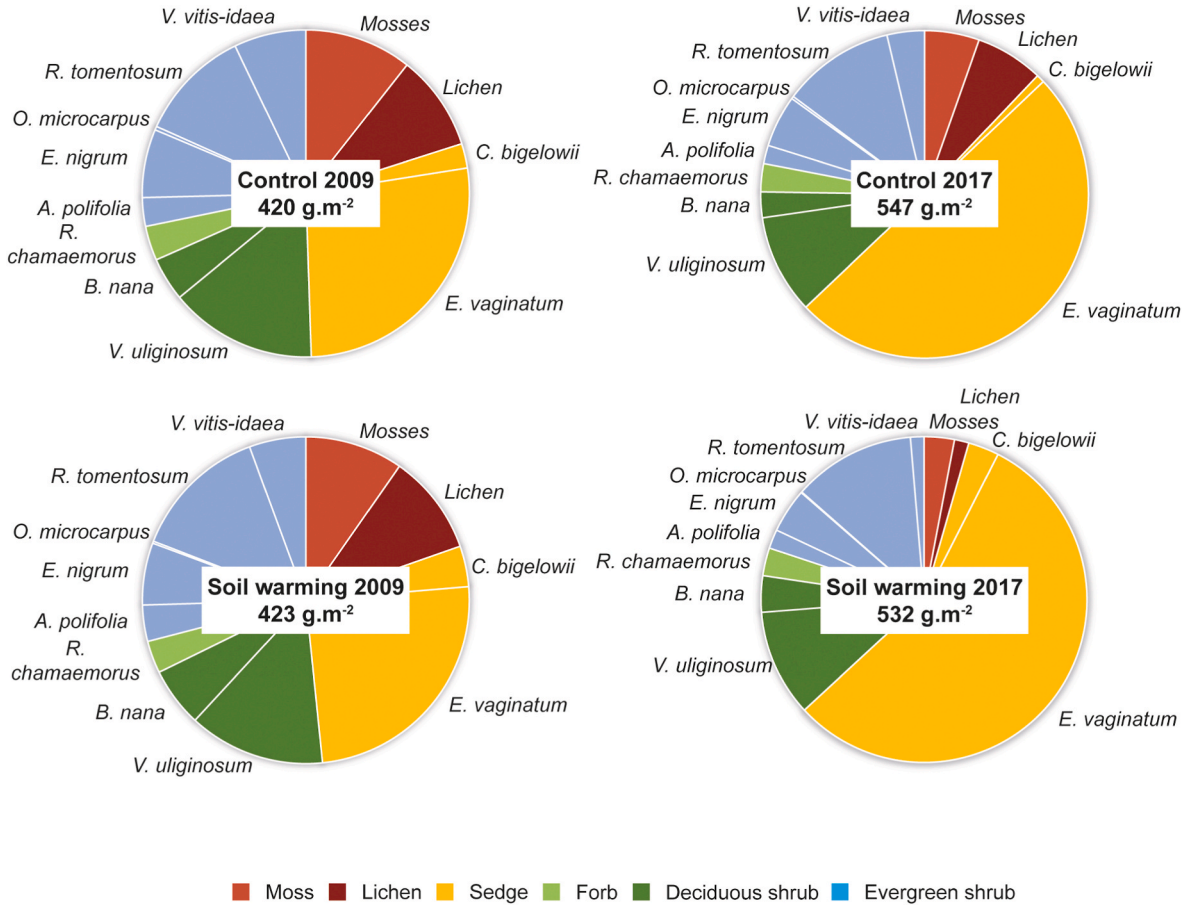

Fig. 1. Foliar biomass composition in the control and soil warming treatments of the CiPEHR experiment between 2009 and 2017. Each pie chart represents the total foliar biomass (g m^{-2}) per treatment and year. Plant functional groups (colors): sedges (yellow), deciduous shrubs (dark green), forbs (light green), evergreen shrubs (blue), mosses (light red), and lichens (dark red). Based on data from Kadej et al. (2022). (For interpretation of the references to color in this figure legend, the reader is referred to the Web version of this article.)

2.4. Biomass data treatment

Datasets of vegetation aboveground biomass at CiPEHR site were available for 2009 and 2017 (Kadej et al., 2022). Biomass measurements were conducted in late July of each year using a non-destructive point frame method (Natali et al., 2011, 2012; Schuur et al., 2007; Shaver et al., 2001). Briefly, this method consists in using a 60 × 60 cm frame with an 8 × 8 cm grid, a 1 mm diameter metal rod vertically inserted at 49 grid intersections. For each contact, "hit", the species and tissue type (leaf, stem, or fruit) were recorded. Site-specific allometric equations based on the average number of hits per plot allowed aboveground plant biomass calculations. A detailed description of this method can be found in Natali et al. (2012). Foliar biomasses were obtained after converting aboveground biomass using species-specific ratios (r) (Mauclet et al., 2022; Salmon et al., 2016; Schuur et al., 2007). Detailed explanations of the calculations and species-specific ratios can be found in Mauclet et al. (2022).

All statistical analyses were conducted using R software (R.4.4.1, R Core Team, 2020). Year and treatment effects were tested using two-way ANOVA comparing four groups within each species with year, treatment and their interaction as fixed effects (2009 control, 2009 winter warming, 2017 control, 2017 winter warming). Species differences, pooled across years and treatments, were tested using one-way ANOVA. All ANOVA tests were followed by Tukey's HSD post-hoc tests for pairwise comparisons with a significance level set at $\alpha = 0.05$. Prior to analysis, normality was verified on ANOVA residuals using the Shapiro-Wilk test and homoscedasticity using Levene's test. When normality assumptions were violated, natural log transformation was applied. Foliar Sr concentrations of *Vaccinium uliginosum* and *Vaccinium vitis-idaea* required log transformation to meet residual normality; all other variables met assumptions without transformation. Full statistical parameters are available in Supplementary Tables S1 and S2.

2.5. Strontium measurements

2.5.1. Elemental strontium analysis

Total strontium (Sr) concentrations in foliar samples (n = 175) were determined using a non-destructive portable X-ray fluorescence (pXRF) device Niton XL3t GOLDD + Analyzer (Thermo Fisher Scientific, Waltham, USA). Samples were dried and ground before being placed in a circular plastic cap (2.5 cm diameter) with a transparent prolene film (4 μm) at its base to ensure a sample thickness of approximately 1 cm (Ravansari et al., 2020; Ravansari and Lemke, 2018). Measurements were conducted under laboratory conditions with each sample scanned for 90 s. The pXRF-measured concentrations were calibrated against wet chemistry method after alkaline fusion, using inductively coupled plasma optical emission spectroscopy (ICP-OES; iCAP 6500, Thermo Fisher Scientific, Waltham, USA). Calibration included 90 foliar samples (Mauclet et al., 2022; Monhonval et al., 2021), and raw pXRF data were averaged from three measurements to determine mean concentrations and standard deviations for each species. Corrected Sr foliar concentrations for all species are available in Supplementary Table S3.

2.5.2. Strontium isotopes measurements

Strontium isotope ratios (Sr) were analyzed on a subset of foliar samples from each treatment (control and soil warming). For each species, 20 samples were selected with five replicates per treatment per year. Sample preparation took place in a class 100 clean laboratory with laminar flow. Dried and ground vegetation samples containing 250-500 ng of Sr were mineralized by heating at 450 °C, then dissolved in sealed Teflon vials using HF/HNO_3 on a hot plate set to 110 °C. The digested solutions were evaporated to dryness and redissolved in 100 μL of 3 M HNO_3. Sr purification step was achieved using 500 μL of pre-cleaned, Sr-specific resin (50–100 μm, Triskem) loaded on Biorad microspin columns. The elution followed the method described by (Aciego et al., 2009). The total procedural blank accounted for less than 0.1% of the total Sr analyzed per sample. Strontium isotope ratios were measured by Multi-Collector Inductively Coupled Plasma Mass Spectrometry (MC-ICP-MS; Neptune Plus) in wet plasma mode, using a 100 μL/min PFA nebulizer. A typical sensitivity of 8-10V was achieved for 100 ppb Sr samples in 2% HNO_3 matrix. Each sample was measured in triplicate, and results are presented as the $^{87}Sr/^{86}Sr$ ratio. Depending on their ^{87}Sr enrichment, samples will be characterized as "more radiogenic" for high $^{87}Sr/^{86}Sr$ ratio and "less radiogenic" for low $^{87}Sr/^{86}Sr$ ratio. NIST SRM 987 reference material was used to validate both column chemistry and analytical precision ($^{87}Sr/^{86}Sr = 0.710269 \pm 0.000059$, 2SD, n = 27). All $^{87}Sr/^{86}Sr$ data measured in plants for this study are available in Supplementary Table S4.

2.6. Modelling soil-plant Sr cycling using $^{87}Sr/^{86}Sr$

To quantify the relative contributions of biocycling and water table rise to the observed changes in plant nutrient sources, we developed a model that simulates Sr transfer within the soil–plant system and tracks the subsequent evolution of $^{87}Sr/^{86}Sr$ in different soil and foliar compartments at the plot scale (Fig. 2). All equations and system components used in this model are reported in Table 1.

In this model, the yearly evolution of Sr stock within each compartment (e.g., plant, soil layer, litterfall) over time is governed by the following equation (Eq. (1)):

$$N(y+1) = N(y) + \sum F_{in} - \sum F_{out} \quad (1)$$

$N(y+1)$ and $N(y)$ are the total mass of Sr in year y+1 and y, while $\sum F_{in}$ and $\sum F_{out}$ represent the total input and output flux to the compartment. Because there is no isotopic fractionation of $^{87}Sr/^{86}Sr$ during soil/plant interaction, the evolution of the $^{87}Sr/^{86}Sr$ ratio in each compartment can be expressed as the isotopic mixing driven by Sr inputs and outputs:

$$r(y+1) = \frac{N(y) \times r(y) + \sum (F_{in} \times r_{in}) - \sum (F_{out} \times r_{out})}{N(y+1)} \quad \text{(Eq 2)}$$

With $r(y+1)$ and $r(y)$ representing the $^{87}Sr/^{86}Sr$ ratio of the modelled compartment at year y+1 and y, respectively and $r_{in/out}$ representing the isotopic ratio of the input and output Sr fluxes.

2.6.1. Plants

The model includes the four plant species used in this study: *Vaccinium vitis-idaea* (P1), *Betula nana* (P2), *Vaccinium uliginosum* (P3), and *Eriophorum vaginatum* (P4) that acquire Sr from the exchangeable soil fraction (Drouet et al., 2007). The soil was divided into three layers chosen to reflect plant rooting and uptake depths (Iversen et al., 2015; Mauclet et al., 2023a,b): S1 (0-5 cm), S2 (5-30 cm), and S3 (30-50 cm).

The yearly evolution of Sr stock in plants is described using the following mass balance equation

$$N_{Pn}(y+1) = N_{Pn}(y) + F_{uptake.Pn} - F_{litterfall.Pn} \quad \text{(Eq 3)}$$

$N_{Pn}(y+1)$ and $N_{Pn}(y)$ represents the stock of Sr in a plant species P_n at year $y+1$ and y, respectively. Plant Sr outputs ($F_{litterfall.Pn}$) are determined by leaf senescence calculated as a fraction of the standing plant Sr stock (k_{Pn}) transferred to the litterfall layer (L_n).

$$F_{litterfall.Pn} = k_{Pn} \times N_{Pn}(y) \quad \text{(Eq 4)}$$

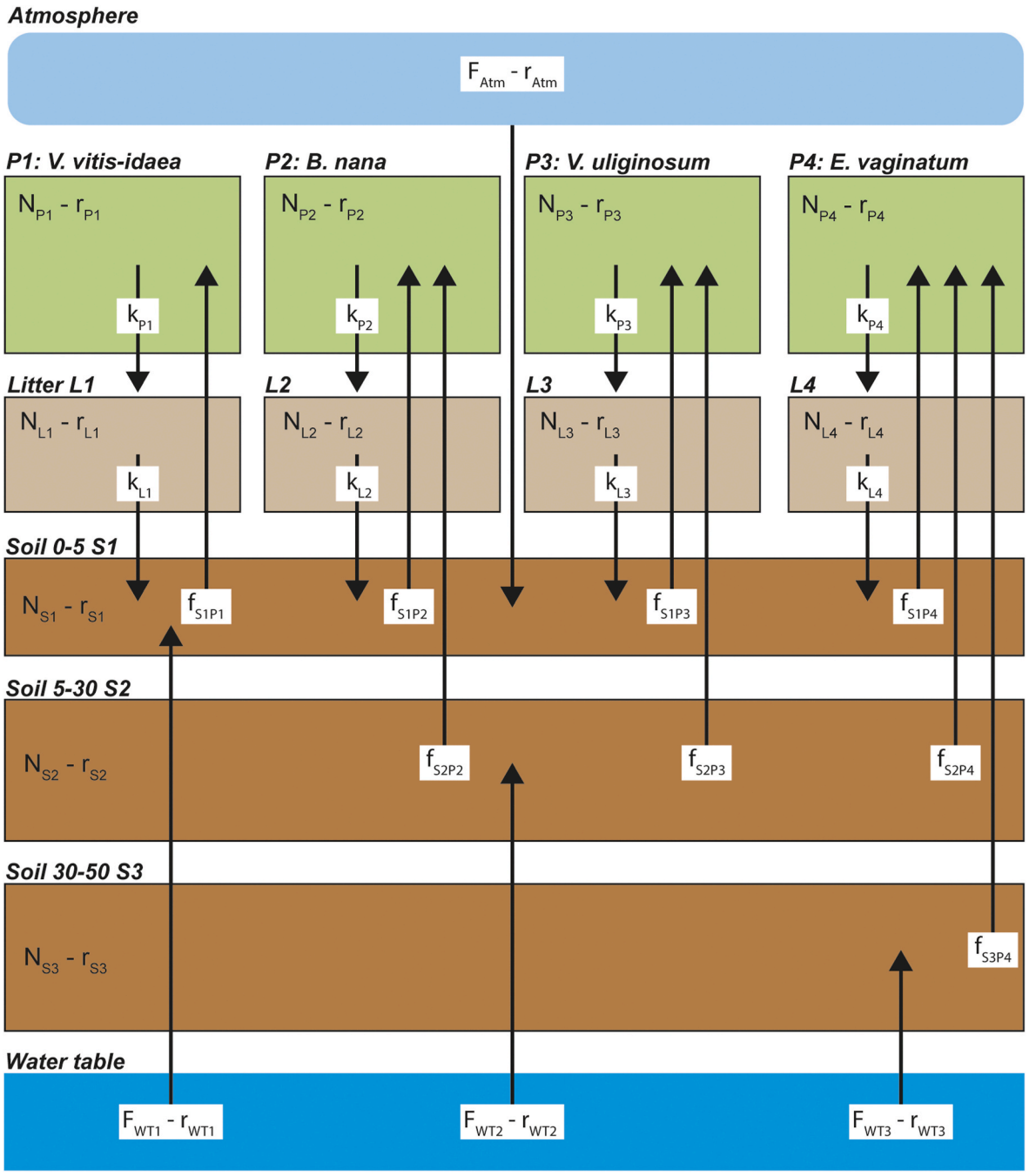

Fig. 2. *Conceptual diagram of a soil-plant cycling model based on strontium and $^{87}Sr/^{86}Sr$ ratio dynamics. The model includes four plant species: Vaccinium vitis-idaea (P1), Betula nana (P2), Vaccinium uliginosum (P3), and Eriophorum vaginatum (P4). Plants take up Sr from the exchangeable fraction of different soil layers (S1: 0–5cm, S2: 5–30cm, S3: 30–50cm). Biocycling is considered through mineralization of the litterfall layer, specific to each species. Water table rise is also considered through fluxes in the different soil layers.*

Plant Sr inputs (F_{uptake}) are defined as the sum of Sr absorbed by roots in each soil layer, factoring in the relative distribution of rooting depths (f_{S1Pn}; f_{S2Pn}; f_{S3Pn}).

$$F_{uptake.Pn} = \sum_{x=1}^{3} k_{SxPn} \times \left(k_{Pn} \times N_{Pn}(y) + F_{growth.Pn}\right) \quad \text{(Eq 5)}$$

F_{uptake} also includes plant growth (F_{growth}), which is assumed to evolve linearly between 2009 ($N_{Pn}(2009)$) and 2017 ($N_{Pn}(2017)$). This is due to limited data availability and allows us to maintain model simplicity.

$$F_{growth} = \frac{N_{Pn}(2017) - N_{Pn}(2009)}{8} \quad \text{(Eq 6)}$$

Because the sum of the relative distribution of rooting depth equals one ($\sum_{x=1}^{3} f_{SxPn} = 1$), the yearly evolution of total Sr stock in plants simplifies to:

$$N_{Pn}(y+1) = N_{Pn}(y) + F_{growth} \quad \text{(Eq 7)}$$

Table 1
Definitions for equation and system components for the soil-plant Sr cycling model.

Equation components	
N	Stock
R	Isotopic ratio
F	Flux
f	Relative rooting depth distribution
k	Turnover rate
t	Time
System components	
Pn	Plant
Ln	Litterfall layer
S_1	0-5 cm soil layer
S_2	5-30 cm soil layer
S_3	30-50 cm soil layer
Atm	Atmosphere
WT	Water table

The evolution of plant $^{87}Sr/^{86}Sr$ ratio can therefore be described using Eq. 8

$$r_{Pn}(y+1) = \frac{(1-k_{Pn})\times N_{Pn}(y)\times r_{Pn}(y) + \left(k_{Pn}\times N_{Pn}(y) + F_{growth.Pn}\right)\sum_{x=1}^{3} f_{SxPn}\times r_{Sx}(y)}{N_{Pn}(y+1)} \quad \text{(Eq 8)}$$

With r_{Pn} and r_{Sx} representing the $^{87}Sr/^{86}Sr$ ratio of the plant and soil layers, respectively.

Finally, the parameters k_{Pn} and f_{SxPn} are set according to plant functional traits, thus representing interspecific differences in rooting architecture and leaf lifespan.

2.6.2. Litter layer

The litterfall compartment (L_n) receives inputs from senescing biomass ($F_{litterfall.Pn}$) before redistribution to the upper soil layer (S_1) through mineralization ($F_{mineralization.Ln}$). The yearly evolution of Sr stock in the litterfall compartment is described using the following mass balance equation:

$$N_{Ln}(y+1) = N_{Ln}(y) + F_{litterfall.Pn} - F_{mineralization.Ln} \quad \text{(Eq 9)}$$

$N_{Ln}(y+1)$ and $N_{Ln}(y)$ represents the stock of Sr in the litterfall layer L_n at year $y+1$ and y, respectively. Plant senescence ($F_{litterfall.Pn}$) is calculated as described in Eq. (4) while Sr outputs through mineralization are modelled as a fraction of the standing litter Sr stock (k_{Ln}), based on interspecific plant litter turnover rate:

$$F_{mineralization.Ln} = k_{Ln}\times N_{Ln}(y) \quad \text{(Eq 10)}$$

Mass balance equation for plant Sr stock can therefore be expressed as follows:

$$N_{Ln}(y+1) = (1-k_{Ln})\times N_{Ln}(y) + k_{Pn}\times N_{Pn}(y) \quad \text{(Eq 11)}$$

The evolution of the litterfall layer $^{87}Sr/^{86}Sr$ ratio can therefore be described using Eq. 12

$$r_{Ln}(y+1) = \frac{(1-k_{Ln})\times N_{Ln}(y)\times r_{Ln}(y) + k_{Pn}\times N_{Pn}(y)\times r_{Pn}(y)}{N_{Ln}(y+1)} \quad \text{(Eq 12)}$$

With $r_{Ln}(y+1)$ and $r_{Ln}(y)$ respectively representing the $^{87}Sr/^{86}Sr$ ratio of the litterfall layer at year $y+1$ and y.

2.6.3. Soil

The upper soil layer S_1 receives Sr input from atmospheric deposition (F_{atm}), the litter layer (L_n), and water table rise (F_{WT1}) while the Sr supply to S_2 and S_3 soil layer is exclusively controlled by the water table (F_{WT2}, F_{WT3}), if any. Plant uptake is the only Sr output from soil layers S_1, S_2 and S_3. The evolutions in Sr stock each soil layer is described using Eq. (13) through Eq. (18).

$$N_{S1}(y+1) = N_{S1}(y) + \sum_{n=1}^{4} F_{mineralization.Ln} + F_{atm} + F_{WT1} - \sum_{n=1}^{4}\left(f_{S1Pn}\times F_{uptake.Pn}\right) \quad \text{(Eq 13)}$$

Table 2
Initial and fixed parameters for the soil-plant Sr cycling model under control and soil warming conditions. Values in parentheses are uncertainties set for the Montecarlo simulation.

Soil		*S1 (0-5 cm)*	*S2 (5-30 cm)*	*S3 (30-50 cm)*	
	N ($\mu g.m^{-2}$)	12000[a]	260000[a]	770000[a]	
	R	0.71218[a]	0.71013[a]	0.70913[a]	
Plants - Control		*P1 (VVi)*	*P2 (BN)*	*P3 (VUG)*	*P4 (EV)*
	N_i ($\mu g.m^{-2}$)	146	135	366	591
	N_f ($\mu g.m^{-2}$)	87	107	277	1346
	R_i	0.71176	0.71092	0.71107	0.70996
	f_{S1}	0.91	0.38	0.46	0.03
	f_{S2}	0.09	0.62	0.54	0.74
	f_{S3}	-	-	-	0.23
	k_{Pn} (yr^{-1})	0.4 (0.1)	1	1	0.33 (0.17)
Plants - Winter warming					
	N_i ($\mu g.m^{-2}$)	106	181	313	537
	N_f ($\mu g.m^{-2}$)	32	154	285	1447
	R_i	0.71162	0.71077	0.71108	0.70988
	k_{S1}	0.85	0.31	0.46	0.03
	k_{S2}	0.15	0.69	0.54	0.67
	k_{S3}	-	-	-	0.30
	k_{Pn} (yr^{-1})	0.4 (0.1)	1	1	0.33 (0.17)

[a] Data from Mauclet et al., 2023a,b

$$N_{S2}(y+1) = N_{S2}(y) + F_{WT2} - \sum_{n=1}^{4}\left(f_{S2Pn} \times F_{uptake.Pn}\right) \quad \text{(Eq 14)}$$

$$N_{S3}(y+1) = N_{S3}(y) + F_{WT3} - \sum_{n=1}^{4}\left(f_{S3Pn} \times F_{uptake.Pn}\right) \quad \text{(Eq 15)}$$

After substitution, we obtain:

$$N_{S1}(y+1) = N_{S1}(y) + \sum_{n=1}^{4}\left(k_{Ln} \times N_{Ln}(y)\right) + F_{atm} + F_{WT1} - \sum_{n=1}^{4}\left(f_{S1Pn} \times \left(k_{Pn} \times N_{Pn}(y) + F_{growth.Pn}\right)\right) \quad \text{(Eq 16)}$$

$$N_{S2}(y+1) = N_{S2}(y) + F_{WT2} - \sum_{n=1}^{4}\left(f_{S2Pn} \times \left(k_{Pn} \times N_{Pn}(y) + F_{growth.Pn}\right)\right) \quad \text{(Eq 17)}$$

$$N_{S3}(y+1) = N_{S3}(y) + F_{WT3} - \sum_{n=1}^{4}\left(f_{S3Pn} \times \left(k_{Pn} \times N_{Pn}(y) + F_{growth.Pn}\right)\right) \quad \text{(Eq 18)}$$

$N_{S1}(y)$, $N_{S2}(y)$ and $N_{S3}(y)$ represent the Sr stocks of soil layers S_1, S_2 and S_3 at year y, respectively. $N_{S1}(y+1)$, $N_{S3}(y+1)$ and $N_{S3}(y+1)$ represent their corresponding value at year $y+1$. The evolution of each soil layer $^{87}Sr/^{86}Sr$ ratio can therefore be described using Eq. (19) through Eq. (21).

$$r_{S1}(y+1) = \frac{\left(r_{S1}(y) \times \left[N_{S1}(y) - \sum_{n=1}^{4}\left(f_{S1Pn} \times \left(k_{Pn} \times N_{Pn}(y) + F_{growth.Pn}\right)\right)\right] + \sum_{n=1}^{4}\left(k_{Ln} \times N_{Ln}(y) \times r_{Ln}(y)\right) + F_{atm} \times r_{atm} + F_{WT1} \times r_{WT1}\right)}{N_{S1}(y+1)} \quad \text{(Eq 19)}$$

$$r_{S2}(y+1) = \frac{r_{S2}(y) \times \left[N_{S2}(y) - \sum_{n=1}^{4}\left(f_{S2Pn} \times \left(k_{Pn} \times N_{Pn}(y) + F_{growth.Pn}\right)\right)\right] + F_{WT2} \times r_{WT2}}{N_{S2}(y+1)} \quad \text{(Eq 20)}$$

$$r_{S3}(y+1) = \frac{r_{S3}(y) \times \left[N_{S3}(y) - \sum_{n=1}^{4}\left(f_{S3Pn} \times \left(k_{Pn} \times N_{Pn}(y) + F_{growth.Pn}\right)\right)\right] + F_{WT3} \times r_{WT3}}{N_{S3}(y+1)} \quad \text{(Eq 21)}$$

$r_{S1}(y)$, $r_{S2}(y)$ and $r_{S3}(y)$ represent the $^{87}Sr/^{86}Sr$ ratio of S_1, S_2 and S_3 at year y, respectively, while $r_{S1}(y+1)$, $r_{S3}(y+1)$ and $r_{S3}(y+1)$ represent their corresponding value at year $y+1$. r_{atm} and r_{WTx} represent the $^{87}Sr/^{86}Sr$ ratio of the atmospheric and water table flux, respectively.

2.7. Parametrization and modelling scenarios

2.7.1. Modelling scenarios

To quantify the relative influence of biocycling and hydrology on the observed foliar $^{87}Sr/^{86}Sr$ shift (2009 – 2017), we implemented four targeted modelling scenarios (Table 3). The first scenario (Sc. 1) acts as a baseline, evaluating the impact of biocycling without warming or water-table inputs. The second scenario (Sc. 2) adds the effect of warming on biocycling processes. The third scenario (Sc. 3) adds the effect of various levels of water table rise to baseline biocycling. The fourth scenario (Sc. 4) combines accelerated biocycling and water table rise.

We note that in all scenarios involving water table rise (Sc. 3 and Sc. 4), biocycling processes remain active, as they are inherently linked to the recorded changes in community composition and productivity at the site (Fig. 1; Kadej et al., 2022). There is therefore no "water-table-only" scenario as it is systematically evaluated in combination with baseline biocycling.

2.7.2. Fixed model parameters

The parameters fixed across all simulation runs are listed in Table 2. Soil parameters (N, r) and atmospheric fluxes (F_{atm}) are set for all scenarios.

Soil layers initial Sr stock and isotopic ratios were calculated as the weighted average of data collected by Mauclet et al. (2023) at the Eight Mile Lake study site, near the CiPEHR experiment. Briefly, exchangeable cations were extracted from <2 mm sieved soil using 1 M ammonium acetate (NH_4OAc) buffered at pH 7, targeting cations held by electrostatic interactions on soil exchange surfaces. The model's S_1, S_2 and S_3 initial values were calculated as weighted average of the different soil

Table 3
Adjustable parameters for each scenario in the soil-plant Sr cycling model and scenario-treatment mapping. Values in parentheses are uncertainties set for the Montecarlo simulation.

		Scenario 1	Scenario 2	Scenario 3a	Scenario 3b	Scenario 4
Biocycling[a]	k_{L1} (yr^{-1})	0.155 (0.050)	0.217 (0.070)	0.155 (0.050)	0.155 (0.050)	0.217 (0.070)
	k_{L2} (yr^{-1})	0.200 (0.030)	0.280 (0.042)	0.200 (0.030)	0.200 (0.030)	0.280 (0.042)
	k_{L3} (yr^{-1})	0.220 (0.060)	0.308 (0.084)	0.220 (0.060)	0.220 (0.080)	0.308 (0.112)
	k_{L4} (yr^{-1})	0.140 (0.080)	0.196 (0.112)	0.140 (0.080)	0.140 (0.060)	0.196 (0.084)
Water table rise[b]	F_{WT1} (µg yr^{-1})	0	0	0	500 (250)	500 (250)
	F_{WT2} (µg yr^{-1})	0	0	2500 (1250)	2500 (1250)	2500 (1250)
Scenario-treatment	Control	x		x		
	Winter warming	x	x	x	x	x

[a] Data averaged over published value; see Supplementary Table 5 for details.
[b] Data based on field observations of water table data (Warren et al., 2025) & porewater Sr concentrations at the nearby Eight Mile Lake gradient site (Opfergelt et al., 2021); see Section 2.7.3. for details.

layers corresponding to the ones in our model. When a soil layer depth interval didn't correspond exactly to our model, we only accounted for the fraction of that layer that was comprised in it (i.e. using only 50% of a soil layer 35-45 cm from the raw dataset in our modelled S_2).

Plants initial and final Sr stock within each plot were derived from foliar biomass estimates as calculated in Mauclet et al. (2022). 2009 and 2017 foliar biomass define N_i and N_f in Eq. (6) and are held constant for each species and treatment (Fig. 1; Table 2).

Atmospheric flux was determined based on Sr measurements in rain on the same study site combined with the average yearly rainfall, yielding an overall flux of approximately 300 $\mu g\ m^{-2}$. This study utilizes *Flavocetraria cucullata*, which is a widespread lichen species in Arctic tundra ecosystems known as a bioindicator of atmospheric composition for atmospheric $^{87}Sr/^{86}Sr$ ratio ($r_{atm} = 0.71133$).

Relative distribution of rooting depths f were derived using mass balance equations between soil layers exchangeable fraction and foliar $^{87}Sr/^{86}Sr$ ratio data measured in 2009. Because uptake doesn't discriminate Sr isotopes, foliar $^{87}Sr/^{86}Sr$ must equal the weighted average of the exchangeable $^{87}Sr/^{86}Sr$ of the accessed soil layers (Capo et al., 1998; Chadwick et al., 1999). Therefore, for P_1-P_3, a two-endmember mixing between S_1 and S_2 was solved. The deeper root distribution of P_4 (*Eriophorum vaginatum*) required solving for all three soil layers (Iversen et al., 2015; Mauclet et al., 2023a,b). To do so, we combined soil layers S_1 and S_2 to determine f within soil layer S_3 before dividing the remaining distribution between S_1 and S_2. We assume relative distribution of roots to be constant through time in order to assess the effects of biocycling and water table rise independently.

Leaf turnover rates (k_{Pn}) were chosen to reflect each species functional type with increasing value from deciduous shrub (annual) to sedge (perennial) to evergreen shrub (perennial). The value of for *Vaccinium vitis-idaea* (0.4 yr^{-1}) corresponds to an average leaf lifespan of approximately 2.5 years, consistent with reported evergreen leaf longevity (Karlsson, 1992), The longer turnover rate time for *Eriophorum vaginatum* is based on the combined effect of internal nutrient translocation occurring during senescence, leaf persistence on the tussock after senescence and tussock longevity (Aerts, 1991, 2008; Shaver and Chapin, 1991).

2.7.3. Adjustable model parameters

The effect of biocycling was evaluated through manipulation of the litter turnover rate k_{Ln}. This parameter was set according to studies conducted with litter from the same species (Demarco et al., 2014; Gao et al., 2022; Hicks Pries et al., 2013; Hobbie, 1996; McLaren et al., 2017; Song et al., 2018). Litter turnover rates were therefore lower for deciduous shrubs than for evergreen shrubs and sedges. The effect of warming (Sc.2 and 4) was tested based on previous studies showing it to accelerate leaf litter turnover by 40% after 150 days (Hobbie, 1996), provided soil moisture levels remain sufficient (Aerts, 2006; Demarco et al., 2014). All set values and associated standard deviations are reported in Table 3.

For the water table rise, we evaluate two hydrology cases that differ by the highest soil layer reached: scenario 3a where the water table reaches S_2 only and scenario 3b where it reaches S_1.For the flux value, the model incorporates Sr inputs (F_{WT1} and F_{WT2}) based on whether field observations show the water table reaching a given soil layer (Supplementary Figs. S1 and S2). When this criterion is met, we then impose a constant yearly flux during the entire simulation period for a given scenario. The value of F_{WT} in each soil layer was estimated from water-table data (Warren et al., 2025) combined with porewater Sr concentrations measured at the nearby Eight Mile Lake gradient site (Opfergelt et al., 2021), and published porosity for organic and mixed soil layers (Letts et al., 2000; Hossain et al., 2015). For each consecutive WTD measurement, ascendant water table movements were identified in each soil layer. These data were then summed over the entire available recording period to obtain the total water table rise for each sampling year. This value was then converted into Sr flux through combination with the mean porewater Sr concentration (Opfergelt et al., 2021) and porosity of each soil layer. Effective porosity was set at 0.9 for S_1 (organic horizon; Letts et al., 2000) and 0.6 for S_2 (mixed organic-mineral horizon; Hossain et al., 2015). Porewater Sr concentrations were $7.3 \pm 5.5\ \mu g\ L^{-1}$ for 0–5 cm depth ($n = 16$) and $9.8 \pm 10.2\ \mu g\ L^{-1}$ for 5–30 cm depth ($n = 64$). the resulting annual Sr flux ranges span 2–65 $\mu g\ m^{-2}\ yr^{-1}$ for S_1 and 0–4746 $\mu g\ m^{-2}\ yr^{-1}$ for S_2 under control conditions, and 45–910 $\mu g\ m^{-2}\ yr^{-1}$ for S_1 and 0–2979 $\mu g\ m^{-2}\ yr^{-1}$ for S_2 under winter warming. For the model, values were therefore set approximately at the midpoint of each treatment, except for F_{WT1} in control conditions, as water rarely reached that soil layer.

The Sr isotopic ratios of the water-table-rise flux are defined by the isotopic composition of the exchangeable Sr fraction of the immediate underlying soil layer; therefore, r_{WT1} and r_{WT2} reflect the isotopic composition of the S_2 and S_3 soil layers, respectively.

2.7.4. Scenario-treatment mapping

A summary of the scenario-treatment mapping is available in Table 3. Based on scenario definitions and the 2009–2017 water-table depth data (Supplementary Figs. S1 and S2), control plots are evaluated under Sc. 1 (baseline biocycling) and Sc. 3a (water-table rise reaching S_2). Because there is no warming Sc. 2 and Sc. 4 does not apply. Soil-warming plots are additionally evaluated under Sc. 2 (accelerated biocycling), Sc. 3b (water-table rise reaching S_1) and Sc. 4 (combined accelerated biocycling and water table rise).

2.8. Model sensitivity analysis

To quantify how uncertainty in biocycling and water table parameters affect modelled foliar $^{87}Sr/^{86}Sr$, we performed a Monte Carlo uncertainty propagation analysis ($n = 100000$). Specifically, we evaluated the influence of litter turnover rates (k_{Ln}), leaf turnover rate (k_{Pn}) and water table rise fluxes (F_{WT}). For each parameter, values were drawn from a normal distribution defined by the reference value and a standard deviation based on published data. For leaf turnover, deciduous species were not tested as their leaves shed annually. The values for *Vaccinium vitis-idaea* were set to 25% to reflect the uncertainty evergreen leaf longevity and at 50% for *Eriophorum vaginatum* to reflect uncertainty in foliar Sr turnover resulting from nutrient resorption as well as tussock and leaf longevity (Aerts, 1991, 2008; Shaver and Chapin, 1991). For water table data, a 50% standard deviation was applied around the set values. The full dataset of reference values and uncertainties are available in Tables 2 and 3

We ran three Monte Carlo sets: (i) biocycling parameters only (k_{Ln} and k_{Pn}), (ii) water table rise only (F_{WT}), and (iii) both sets of parameters simultaneously. For each set, we recorded simulated 2017 foliar $^{87}Sr/^{86}Sr$ for each species for each simulated year between 2009 and 2017 and the results are shown as 1SD band around the modelled value.

Rooting distribution fractions (f) were not included in the Monte Carlo analysis because they are not free parameters in our model but rather solved from the isotopic mass balance between 2009 foliar $^{87}Sr/^{86}Sr$ and soil exchangeable $^{87}Sr/^{86}Sr$ endmembers (See Section 2.7.2 for details). Varying f independently of the soil endmembers would therefore violate mass-balance consistency.

3. Results

3.1. Foliar Sr concentrations

Average foliar Sr concentrations exhibited a consistent decreasing trend in the order *Betula nana* > *Vaccinium uliginosum* > *Eriophorum vaginatum* > *Vaccinium vitis-idaea*, regardless of treatment or year considered (Fig. 3a). Statistical analysis confirmed significant differences at the species level, with *Betula nana* exhibiting the highest Sr concentration ($7.58 \pm 1.63\ mg\ kg^{-1}$, $n = 38$), followed by *Vaccinium*

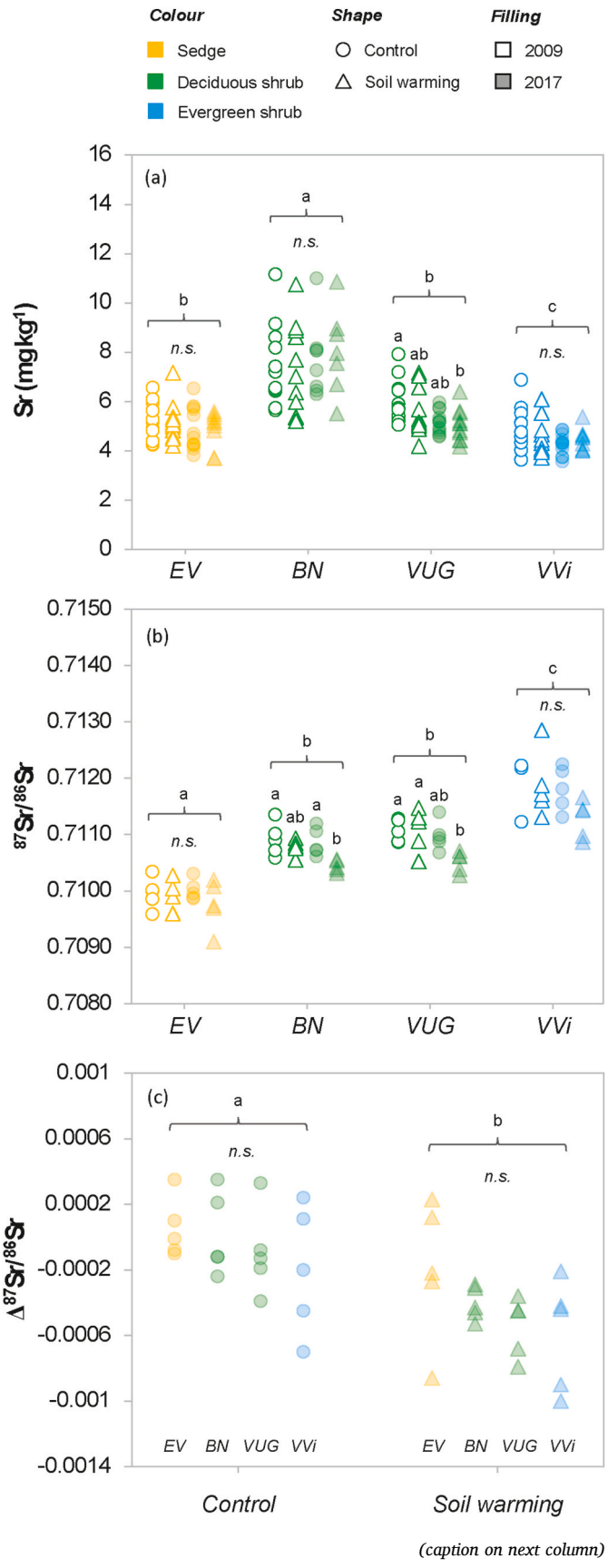

(caption on next column)

Fig. 3. Comparison of Sr concentration and isotopic composition among *Eriophorum vaginatum* (EV), *Betula nana* (BN), *Vaccinium uliginosum* (VUG), and Vaccinium vitis-idaea (VVI) across treatments and sampling years. (a) Sr concentrations ($mg{\cdot}kg^{-1}$), (b) $^{87}Sr/^{86}Sr$ ratios, and (c) relative changes in $^{87}Sr/^{86}Sr$ ratios between 2017 and 2009 ($\Delta^{87}Sr/^{86}Sr$). Shapes, filling and colors represent treatments, sampling year, and plant functional groups, respectively. In panels (a) and (b), within-species differences across the four Year × Treatment cells were tested using a two-way ANOVA followed by Tukey HSD ($\alpha = 0.05$). Differences between species (pooled across years and treatments) were tested using a one-way ANOVA followed by Tukey HSD. In panel (c), the overall treatment effect was tested using a one-way ANOVA on $\Delta^{87}Sr/^{86}Sr$ pooled across species. Statistical significance is indicated by letters above data points. (For interpretation of the references to color in this figure legend, the reader is referred to the Web version of this article.)

uliginosum (5.43 ± 0.82 mg kg^{-1}, n = 47) and *Vaccinium vitis-idaea* (4.52 ± 0.67 mg kg^{-1}, n = 45). *Eriophorum vaginatum* showed no significant differences in foliar Sr concentrations, with values overlapping those of both *Vaccinium* species (5.05 ± 0.77 mg kg^{-1}, n = 45). Although the overall pattern was consistent across treatments and sampling years, statistical significance was not consistently observed across species.

Foliar Sr concentrations in the 2009 control treatment decreased from 7.50 ± 1.58 mg kg^{-1} (*Betula nana*, n = 12) to 4.48 ± 0.87 mg kg^{-1} (*Vaccinium vitis-idaea*, n = 12). Similar values were observed for the soil warming treatment, thus indicating similar intraspecies variability at the start of the experiment. This pattern persisted in 2017 with *Vaccinium vitis-idaea* again showing the lowest foliar Sr concentration in the control treatment (4.26 ± 0.42 mg kg^{-1}, n = 12) and *Betula nana* under soil warming exhibiting the highest value (8.03 ± 1.72 mg kg^{-1}, n = 7). Across all species and treatments, foliar Sr concentrations ranged between 3.56 and 11.16 mg kg^{-1}.

Overall, the two-way ANOVA revealed no significant effects of Treatment or Year × Treatment interaction on foliar Sr concentrations for any of the four species (Supplementary Table S2). A significant Year main effect was detected only for *Vaccinium uliginosum*, reflecting a decrease in concentrations between 2009 and 2017 in both control and warming plots rather than a treatment effect.

3.2. Foliar $^{87}Sr/^{86}Sr$ ratios

The $^{87}Sr/^{86}Sr$ ratios of foliar tissues of the four studied vascular plants ranged from 0.70910 to 0.71260 (Fig. 3b). Overall, the data exhibited a pattern similar to that of Sr concentrations, with distinct values among species and consistent trends across treatments and sampling years. At the species level, $^{87}Sr/^{86}Sr$ ratios decreased from *Vaccinium vitis-idaea* (0.711148 ± 0.00052, n = 20) to *Eriophorum vaginatum* (0.70990 ± 0.00030, n = 20). *Betula nana* and *Vaccinium uliginosum* exhibited intermediate values of 0.71075 ± 0.00027 (n = 20) and 0.71091 ± 0.00034, respectively. Statistical analysis confirmed significant differences at the functional group level among evergreen, deciduous, and sedge species, though significance was occasionally lost when data were analyzed by treatment and/or sampling year. Nevertheless, the observed pattern of data is within the range reported for the same plant species measured at the nearby permafrost thaw gradient, excluding *Vaccinium uliginosum* (Mauclet et al., 2023a,b).

The two-way ANOVA showed no statistical differences among species between control and soil warming treatments in 2009, thus confirming similar intraspecies variability at the start of the experiment (Supplementary Table S2). The largest difference in $^{87}Sr/^{86}Sr$ ratios between treatments, 0.00014, was observed for *Betula nana* and *Vaccinium vitis-idaea*. In 2017, $^{87}Sr/^{86}Sr$ ratios under the soil warming treatment appeared systematically lower than under control treatment for all four plants, with average differences ranging from 0.00025 in *Eriophorum vaginatum* to 0.00060 in *Vaccinium vitis-idaea*. Significant pairwise differences were confirmed for *Betula nana*, with 2017 soil warming lower than both 2009 control and 2017 control, and for *Vaccinium*

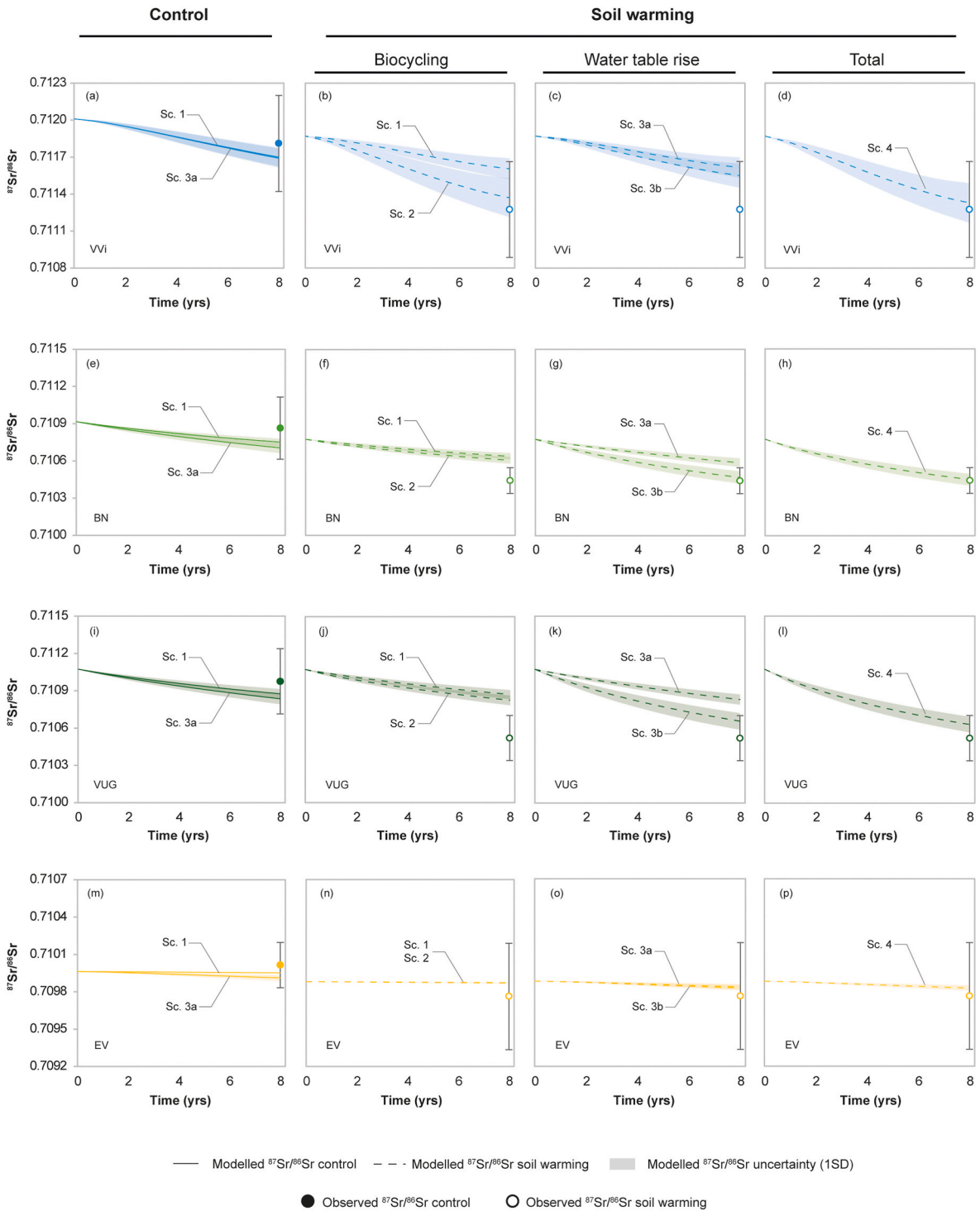

Fig. 4. Modelled and observed foliar $^{87}Sr/^{86}Sr$ ratios over time of Vaccinium vitis-idaea (a-d), *Betula nana* (e-h), *Vaccinium uliginosum* (i-l) and *Eriophorum vaginatum* (m-p) under different Sr cycling scenarios. Sc. 1: Baseline biocycling parameters; Sc. 2: Accelerated biocycling; Sc. 3a: Baseline biocycling + Water table rise into S_2; Sc. 3b: baseline biocycling + Water table flux into S_2 and S_1; and Sc. 4: accelerated biocycling + Water table flux into S_2 and S_1 (details in §2.7). For each species, the first column shows the control treatment (Sc. 1), followed by soil warming under biocycling only (Sc. 1–2), water table rise (Sc. 3a–3b), and combined forcing (Sc. 4). Solid lines represent modelled values; shaded areas represent Monte Carlo uncertainty (1SD); symbols represent observed data. The range of $^{87}Sr/^{86}Sr$ ratios displayed on the y-axis is set to 0.0015 to allow comparison.

uliginosum, with 2017 soil warming lower than both 2009 treatments. *Eriophorum vaginatum* and *Vaccinium vitis-idaea* also showed decrease in 2017 soil warming, but these did not reach significance (Tukey HSD, $p > 0.05$).

A normalization based on the relative difference between plants measured in 2017 and 2009 for both treatments showed that the foliar $^{87}Sr/^{86}Sr$ significantly decreased in the soil warming treatment when all plants are considered (Fig. 3c). This difference follows a similar trend observed across species so far, with $\Delta^{87}Sr/^{86}Sr$ increasing in the order *Eriophorum vaginatum* < *Betula nana* < *Vaccinium uliginosum* < *Vaccinium vitis-idaea,* although species did not differ significantly within both treatments.

3.3. Model results

Model outputs are presented in Fig. 4 based on the fixed and adjustable inputs (Tables 2 and 3).

3.3.1. Scenario 1 - impact of biocycling

Baseline biocycling alone reproduces the slight decline in foliar $^{87}Sr/^{86}Sr$ observed in the control treatment, with simulated values remaining within the standard deviation of the observations across species, although systematically lower (Fig. 4a–e, I, m). Baseline biocycling values are not sufficient to reproduce the isotopic shift observed in the soil warming treatment (Fig. 4b–f, j, n).

3.3.2. Scenario 2 – impact of accelerated biocycling

The 40% increase in litter turnover, consistent with warming responses reported in previous studies, leads to a slightly higher isotopic shift than that of baseline litter turnover values. This shift is the largest in the shallow-rooted *Vaccinium vitis-idaea*, intermediate in *Betula nana* and *Vaccinium uliginosum*, and weakest in the deep-rooted *Eriophorum vaginatum* (Fig. 4b–f, j, n). The large variability for *Vaccinium vitis-idaea* target $^{87}Sr/^{86}Sr$ values allows this scenario to reproduce the observed isotopic shift. However, it fails to reproduce the observed isotopic shift for *Betula nana* and *Vaccinium uliginosum*.

3.3.3. Scenario 3 - impact of water-table rise

Adding a water-table input to S_2 produces marked shifts in $^{87}Sr/^{86}Sr$ foliar ratios for intermediate and deep-rooted species (*Betula nana*, *Vaccinium uliginosum* and *Eriophorum vaginatum*), whereas shallow-rooted *Vaccinium vitis-idaea* shows little impact of an S_2 input alone, regardless of treatment (Fig. 4c–g, k, o). For control plots, Sc. 3a keeps keeps simulated foliar $^{87}Sr/^{86}Sr$ foliar ratios within the observed variability but doesn't improve the fit of Sc. 1, which already reproduces the small isotopic shift. For the soil warming plots, Sc. 3a isn't sufficient to reproduce the shifts for *Betula nana* and *Vaccinium uliginosum* and increasing F_{WT2} further would overshoot the target $^{87}Sr/^{86}Sr$ foliar ratios in the deeper-rooted species under control conditions. Adding an S_1 input (Sc. 3b) therefore allows to reproduce the observed shift in *Vaccinium vitis-idaea* and *Betula nana*. It also partly reproduces the observed shift for *Vaccinium uliginosum*, while *Eriophorum vaginatum* remains largely unchanged due to limited rooting in S_1 (Fig. 4).

3.3.4. Scenario 4 - combined processes

Combining accelerated biocycling with S_1+S_2 water-table inputs (Sc. 4) yields the closest results to the observed foliar $^{87}Sr/^{86}Sr$ ratios, with only small differences relative to Sc. 3b (Fig. 4d–h, l, p). Nevertheless, while the modelled foliar $^{87}Sr/^{86}Sr$ ratio of *Vaccinium uliginosum* is within the observed variability of the target value (1SD), the simulated values are systematically higher than the observed mean, and this offset persists even when accounting for model uncertainty. A similar, though smaller, offset is observed for *Eriophorum vaginatum*, for which the combined scenario accounts for less than half of the observed isotopic shift. Increasing the water table flux to S2 would reduce this discrepancy but would in turn cause the model to overshoot the observed foliar $^{87}Sr/^{86}Sr$ ratios of deeper-rooted species under control conditions.

3.4. Sensitivity analysis and uncertainty results

The Monte Carlo uncertainty propagation ($n = 100000$) revealed marked differences in model sensitivity among species and scenarios (Fig. 4). Across all scenarios, *Vaccinium vitis-idaea* consistently exhibited the largest uncertainty ($1SD = 0.00008–0.00016$), followed by *Vaccinium uliginosum* (0.00004–0.00007), *Betula nana* (0.00003–0.00005) and *Eriophorum vaginatum* (0.000003–0.00002). Under biocycling scenarios (Sc. 1 and Sc. 2), *Eriophorum vaginatum* showed near-zero sensitivity ($1SD \leq 0.000003$), reflecting the negligible influence of leaf and litter turnover uncertainty on this deep-rooted species. Increasing the biocycling acceleration to 40% had a limited effect on output uncertainty, with standard deviations increasing by only 10–20% across all species. In contrast, the inclusion of water table parameters substantially widened the uncertainty envelopes for all species. The addition of the water table flux to S_2 alone increased standard deviations by 15–30% relative to biocycling scenarios, while extending the flux to both S_1 and S_2 approximately doubled the uncertainty for *Vaccinium vitis-idaea* (from 0.00008 to 0.00016), *Betula nana* (from 0.00003 to 0.00005) and *Vaccinium uliginosum* (from 0.00004 to 0.00007). The effect was most pronounced for *Eriophorum vaginatum*, whose standard deviation increased by an order of magnitude when water table parameters were included (from 0.000003 to 0.00002), consistent with its direct access to deeper soil layers where water table fluctuations operate. Overall, the sensitivity analysis indicates that water table flux uncertainty, rather than biocycling parameter uncertainty, is the dominant source of model output variability. Importantly, the uncertainty generated by biocycling parameters alone, or in combination with water table rise, remain largely below the measured intraspecific variability for all species and treatments.

4. Discussion

4.1. Plant nutrient acquisition and soil Sr source traced by $^{87}Sr/^{86}Sr$

Plant demand appears to be the primary factor driving Sr levels in leaves of the four plants studied, since soil warming did not affect foliar Sr concentrations (Fig. 3a). This implies that foliar Sr concentrations reflect distinct uptake and storage strategies among plant functional types. This also implies that Sr nutritional requirements of each species are met throughout the experiment without any adaptive mechanisms despite large differences in soil Sr availability (i.e., the exchangeable soil fraction) and plant rooting depth (Iversen et al., 2015; Mauclet et al., 2023).

Because Sr enters the root system passively, without biological fractionation (Capo et al., 1998; White, 2001), $^{87}Sr/^{86}Sr$ ratios in foliar tissues reflect the weighted average of the soil exchangeable pools accessed by plants (Chadwick et al., 1999; Mauclet et al., 2023a,b; Vitousek et al., 1999). The variations in foliar $^{87}Sr/^{86}Sr$ ratios across species are therefore a consequence of plant accessing distinct base cation pools, due to species specific rooting depth distribution and nutrient acquisition strategies, in accordance with previous studies (Hewitt et al., 2019; Iversen et al., 2015; Mauclet et al., 2023a,b). Importantly, this interspecific variation is larger than treatment effects, indicating that rooting depth classification remains similar throughout the experiment (Iversen et al., 2015; Wang et al., 2017). The differences in foliar $^{87}Sr/^{86}Sr$ ratios among species (Fig. 3b) combined with the decreasing $^{87}Sr/^{86}Sr$ ratios with depth observed in the exchangeable Sr fraction at this site suggests that their nutrient acquisition occurs from different soil horizons (Mauclet et al., 2023a,b). *Vaccinium vitis-idaea*, *Betula nana* and *Vaccinium uliginosum* therefore rely on more radiogenic Sr located in the organic layer while *Eriophorum vaginatum* is taking Sr up from less radiogenic sources in the mineral layer.

While nutrient acquisition strategies remain unchanged between 2017 and 2009 (Fig. 3b), the generalized shift towards less radiogenic foliar $^{87}Sr/^{86}Sr$ ratios in the soil warming treatment is indicative of a shift in nutrient sources for both shallow and deep rooted species in response to permafrost thaw. Root redistribution in response to active layer deepening has been reported for deep-rooted species in permafrost environments (Blume-Werry et al., 2019; Salmon et al., 2016; P. Wang et al., 2017). However, *Eriophorum vaginatum* shows the smallest and non-significant isotopic shift under warming compared to the other shallow and intermediate rooted species (Fig. 3b), which suggests that an additional process is required to deliver less-radiogenic nutrients from depth into the shallow soil layers accessed by these species.

4.2. Process controls on the observed foliar $^{87}Sr/^{86}Sr$ shift

Several mechanisms have been suggested to drive the foliar $^{87}Sr/^{86}Sr$ decrease in all plant functional groups (Mauclet et al., 2023). Firstly, rooting depth changes due to permafrost thaw allows plants to access deeper soil layers containing base cation pools with lower radiogenic Sr (Mauclet et al., 2023a,b). However, this process is mostly impacting deep-rooted plants (Blume-Werry et al., 2019; Wang et al., 2017), yet the isotopic shift is observed across all species, which suggests additional processes allowing for Sr transfer from deep soil layers.

Secondly, shifts in the plant community composition could also modify the $^{87}Sr/^{86}Sr$ ratio of the exchangeable soil fraction throughthe biocycling loop. Deep-rooted *Eriophorum vaginatum* takes up nutrients from deeper, less-radiogenic pools (Fig. 3b; Mauclet et al., 2023a,b; Iversen et al., 2015), incorporates it into foliar biomass, and returns it to the surface organic layer through litterfall, where mineralization releases the Sr into the upper exchangeable pool lowering its $^{87}Sr/^{86}Sr$ ratio. Shallow and intermediated rooted plants subsequently take up Sr from this same upper exchangeable pool, thus propagating the isotopic shift into their foliar tissues. This is supported by the expansion of *Eriophorum vaginatum*, whose relative biomass increased from 85% to 125% under soil warming (Fig. 1), and therefore drives the biocycling signal in the model. However, while baseline biocycling is sufficient to explain the small shift in foliar $^{87}Sr/^{86}Sr$ ratio (Fig. 4a–c, e, g), an imposed 40% increase in litter turnover remains insufficient to match the warming-treatment shift in foliar $^{87}Sr/^{86}Sr$ ratio (Fig. 4b–d, f, h). Taken together, this suggests that biocycling clearly contributes to the upward transfer of deeper nutrients but is insufficient on its own to reproduce the isotopic shift observed under soil warming.

Lastly, water table rise is a well-documented consequence of permafrost thaw, potentially leading to Sr transport from deep soil layers to the surface (Monhonval et al., 2023; Rodenhizer et al., 2020). This process makes deep base cations available to all plant functional groups, regardless of their rooting depth. At the CiPEHR site, water tables under winter warming treatment were consistently closer to the surface than in the control, with statistically significant treatment differences emerging from 2012 onward (Mauritz et al., 2017). This shallower water table under warming allows for episodic contact with the shallow organic horizon (S_1), which is almost absent in control plots (Supplementary Fig. S1). Even modest water table rises can produce measurable isotopic shifts because the exchangeable Sr stock in the shallow organic layers (S_1) is much smaller than in the underlying mixed (S_2) and mineral layers (S_3) and much more radiogenic (Mauclet et al., 2023a,b). A relatively minor influx of less-radiogenic, mineral-derived Sr is therefore sufficient to shift the $^{87}Sr/^{86}Sr$ ratio of the S_1 soil layer within a few years, consistent with the timescale of the observed change (Fig. 3c). In this regard, modelling results (Fig. 4) indicate that baseline biocycling with water table inputs to S_2 keeps the foliar $^{87}Sr/^{86}Sr$ ratio trajectory within observed variability (Fig. 4a–c, e, g) in the control treatment. In the soil warming treatment, however, inputs are required in our simulations to reach all soil layers to reproduce the observed isotopic shift, in accordance with field observations (Supplementary Figs. S1 and S2). This pattern indicates that water table rise acts as an upward transfer of deep nutrients on a much shorter timescale (<10 years), especially when considering that water table rise consistently reached S_1 only in 2012 (Supplementary Fig. S1). Under control conditions, water table contributions (Sc. 3a) generate only marginal additional shifts from the baseline biocycling scenario, with modelled values remaining within the measured standard error in 2017; water table rise can therefore not be ruled out as a secondary process of nutrient redistribution under control conditions. The combined scenario Sc. 4 adds little over Sc. 3b, emphasizing the secondary control of accelerated biocycling over nutrient redistribution at the profile scale.

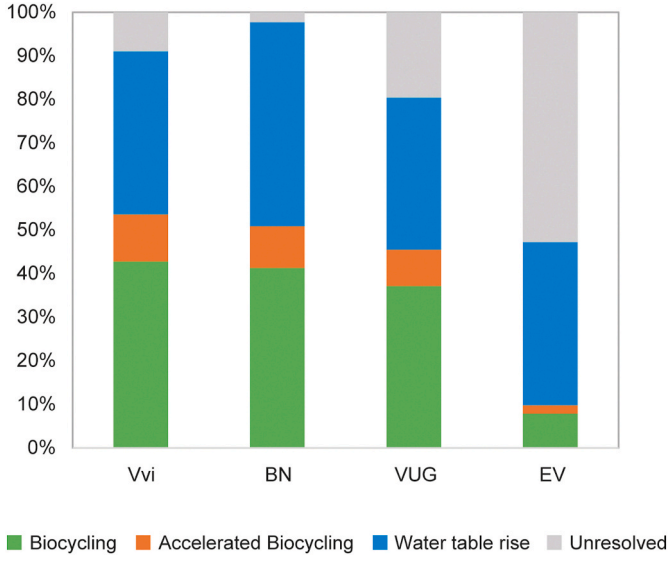

Fig. 5. Relative contribution of biocycling, accelerated biocycling and water table rise to the observed shift in foliar $^{87}Sr/^{86}Sr$ among *Eriophorum vaginatum* (EV), *Betula nana* (BN), *Vaccinium uliginosum* (VUG), and Vaccinium vitis-idaea (VVI) under soil warming treatment.

4.3. Excluded processes

Our model focuses on biocycling and water table rise as the two mechanisms most directly constrainable with our Sr isotope dataset. Several additional processes were not explicitly included. Redox-mediated cation mobilization is closely linked to water table dynamics (Herndon et al., 2020; Monhonval et al., 2023) as well as organic matter decomposition rates (Moore and Dalva, 1993) and are therefore included within the water table flux terms, as the porewater Sr concentrations integrate the geochemical conditions at the water table interface. Changes in rooting depth in response to permafrost thaw primarily affect deep-rooted species such as sedges (Blume-Werry et al., 2019; Wang et al., 2017), while the isotopic shift is observed across all species (Fig. 3b & c). Increased mineral weathering and microbial priming would both require a uniformly less radiogenic Sr source across all soil depths to explain the observed shift, which is inconsistent with the strong vertical geochemical gradients in the soil profile and the changes in dominant mineral phases (Mauclet et al., 2023a,b). Moreover, weathering-driven changes in exchangeable $^{87}Sr/^{86}Sr$ operate on timescales of centuries to millennia (Blum and Erel, 1997; Capo et al., 1998; Chadwick et al., 1999). Enhanced decomposition under warming is implicitly captured through the litter turnover rate, which was increased by 40% in warming scenarios (Hobbie, 1996). We acknowledge that these additional processes likely contribute to nutrient redistribution in thawing permafrost soils but consider them secondary relative to biocycling and water table rise over the timescale of this experiment.

4.4. Relative contributions

Based on our model results, biocycling alone is sufficient to reproduce the observed foliar $^{87}Sr/^{86}Sr$ ratio shift under control conditions, whereas reproducing the warming-treatment shift requires the contribution of water table rise (Fig. 4). The relative contributions each process can therefore be determined by comparing the isotopic shift induced by biocycling, accelerated biocycling, and water table rise to the total measured shift (Fig. 5). Because the model systematically overshoots the measured foliar $^{87}Sr/^{86}Sr$ ratio in 2017 control treatment, we report water table contributions as not estimated, rather than a truncated negative. Biocycling is therefore assumed to possibly explain 100% of the observed isotopic shift. For the soil warming treatment, biocycling accounts for 8 to 43% of the observed shift in foliar $^{87}Sr/^{86}Sr$

ratio, with the highest contributions for shallow and intermediate rooted species (*Vaccinium vitis-idaea*: 43%, *Betula nana*: 41%, *Vaccinium uliginosum*: 36%) and the lowest for *Eriophorum vaginatum* (8%). Accelerated biocycling is responsible for an additional 2% for *Eriophorum vaginatum* to 11% for *Vaccinium vitis-idea.* Water table rise contributes from 35 to 47% of the observed shift in foliar $^{87}Sr/^{86}Sr$ ratio across species. The combined scenario (Sc. 4) explains 91% and 98% of the observed shift for *Vaccinium vitis-idaea* and *Betula nana*, respectively, but only 80% for *Vaccinium uliginosum* and 47% for *Eriophorum vaginatum,* leaving 20% and 53% of the observed shift unaccounted for by the modelled mechanisms. When accounting for model uncertainty (1SD), the Sc. 4 scenario fully encompasses the observed values for *Vaccinium vitis-idaea* and *Betula nana* and reaches up to 91% for *Vaccinium uliginosum* and 65% for *Eriophorum vaginatum*.

Overall, rooting depth and distribution appear to be a primary control on the balance between modelled mechanisms: shallow rooted species benefit mostly from biocycling, while water table contributions are relatively similar across species. The large unresolved shift for *Eriophorum vaginatum* is likely due to the minimal change of foliar $^{87}Sr/^{86}Sr$ ratios between 2009 and 2017, although its low root density in the S_1 soil layer limits the influence of nutrients from biocycling. Nevertheless, the persistent undershoot for *Vaccinium uliginosum* and *Eriophorum vaginatum* suggests that additional processes not captured in the current model may contribute to the observed isotopic shift in these species. These are further discussed in Section 4.5.

4.5. Limitations of the modelling framework

Our results show that *Eriophorum vaginatum* dominates the $^{87}Sr/^{86}Sr$ ratio of the litterfall layer and therefore of biocycling processes, due to it comprising most of the standing biomass between 2009 and 2017 (Fig. 1). Under biocycling-only scenarios, the model systematically overshoots the observed 2017 foliar $^{87}Sr/^{86}Sr$ ratios in the control treatment for all species (Fig. 4). This could reflect an overestimated contribution of deep-rooted litter to topsoil biocycling, given that nutrient dynamics in *Eriophorum vaginatum* tussocks remain poorly constrained. Nutrient translocation to the rhizome during senescence is well documented for this species (Chapin et al., 1979; Jonasson and Stuart Chapin, 1985; 1991; Shaver and Chapin, 1991), dead leaves can remain attached to the tussock for extended periods before entering the soil litter pool, and tussock longevity itself has been estimated at approximately four years (Aerts, 2008). Together, these processes could delay and reduce the transfer of less-radiogenic Sr from *Eriophorum vaginatum* litter to the surface soil.

Conversely, the model underestimates the observed isotopic shift for *Vaccinium uliginosum* and *Eriophorum vaginatum* under soil warming (Fig. 4). This could be due to an underestimation of the Sr flux delivered by water table rise to S_2. Increasing this flux would improve the fit for both species under warming but would simultaneously cause the model to overshoot the observed foliar $^{87}Sr/^{86}Sr$ of deeper-rooted species under control conditions. Root redistribution in response to active layer deepening could also contribute to the undershoot, as deeper root placement would give both species access to less radiogenic Sr pools, although such responses have primarily been documented for deep-rooted sedges (Blume-Werry et al., 2019; Wang et al., 2017). However, these opposing parameters are somewhat linked, as any mechanism that raises foliar $^{87}Sr/^{86}Sr$ in the control would also increase the discrepancy between model and observed data under soil warming.

5. Outlook

Our results suggest that redistribution mechanisms, rather than direct release from thawed permafrost, play a dominant role in shaping plant nutrient availability at this timescale. Biocycling and water table rise operate on complementary timescales and through distinct pathways: biocycling gradually transfers nutrients from deep-rooted litter into the surface organic layers over approximately 10 years, while water table rise delivers dissolved nutrients from mineral horizons directly into the rooting zone over shorter timescales (approx. 1–5 years). Neither mechanism alone is sufficient to explain the observed data under soil warming, and their combined action underscores that nutrient redistribution in thawing permafrost is inherently a multi-process phenomenon.

These mechanisms will not affect all species equally. Shallow-rooted species are most sensitive to biocycling, as nutrient inputs from litter mineralization are concentrated in the surface organic layers where their roots are located. They are also highly responsive to water table rise, because the low exchangeable Sr stock in shallow organic layers makes them sensitive to even small inputs from deeper mineral pools. In contrast, deep-rooted species such as *Eriophorum vaginatum* show limited response to biocycling but may access newly thawed nutrients directly or benefit from hydrological redistribution to deeper soil layers. The sensitivity of each functional group will therefore depend on the balance between rooting depth, litter production, and the extent of water table fluctuations. Future studies incorporating direct measurements of root length and vertical distribution at the species level would further improve our understanding of how rooting architecture shapes nutrient access under permafrost thaw.

Nevertheless, the relative importance of biocycling and water table rise as dominant nutrient uplift mechanism will ultimately depend on the hydrological evolution of permafrost ecosystems (De Vrese et al., 2023). Drier, well-drained landscapes are expected to depend on biocycling for nutrient uplift, whereas lowland thermokarst formations, subsidence-affected regions, and overall wetter ecosystems are likely to be dominated by water table fluctuations, similarly to the results of this study (Osterkamp et al., 2009; Rodenhizer et al., 2020). In the context of a warming Arctic, increasing precipitation and projected permafrost losses are expected to amplify hydrological changes, potentially amplifying the impact of water-table driven nutrient uplift in many ecosystems (McCrystall et al., 2021; Peng et al., 2023).

6. Conclusion

This study combined an eight-year soil warming experiment at the CiPEHR site in Interior Alaska with measurements of foliar Sr concentrations and $^{87}Sr/^{86}Sr$ ratio in four dominant tundra plant species (*Eriophorum vaginatum, Betula nana, Vaccinium uliginosum*, and *Vaccinium vitis-idaea*). We aimed to quantify the relative contribution of biocycling and water table rise to the evolution of plant nutrient sources by modeling Sr cycling in the soil–plant system using mass balance equations.

Our results show a shift in foliar $^{87}Sr/^{86}Sr$ ratio over time which reflects changes in plant nutrient sources that are significantly more pronounced under soil warming. While biocycling successfully explains the data under control conditions, reproducing the observed shift under soil warming requires a large uplift of Sr via water table rise in our model. The combine model (biocycling + water table rise) explains 91-98% of the observed shift for *Vaccinium vitis-idaea* and *Betula nana,* but only 47-80% for *Eriophorum vaginatum* and *Vaccinium uliginosum*. Although all modelled values remain within the observed variability, this discrepancy indicates that additional processes may contribute for these species. Under soil warming, biocycling is responsible for 36-54% of the shift in shallow and intermediate rooted species, while water table accounts for 35-47%. Both mechanisms are essential to reproduce the isotopic shift although they operate on different timescales, with biocycling effects occurring over approximately 10 years while water table rise appears to be quicker, over less than 5 years.

These findings emphasize that redistribution mechanisms are indispensable to allow plants to capitalize on the release of nutrients from permafrost thaw, and that the balance between biocycling and water table rise is controlled by plant functional traits, particularly rooting depth.

Declaration of generative AI and AI-assisted technologies in the writing process

This manuscript has been edited with the help of Claude AI to improve readability, flow, and overall English quality. After using this tool/service, I, the author, reviewed and edited the content as needed. The structure of ideas, argumentative flow and message conveyed by this manuscript remain entirely my own, and I take full responsibility for its content.

CRediT authorship contribution statement

Philippe Roux: Conceptualization, Data curation, Formal analysis, Investigation, Methodology, Writing – original draft. **Damien Lemarchand:** Conceptualization, Investigation, Methodology, Validation, Writing – review & editing. **Edward A.G. Schuur:** Data curation, Resources, Validation, Writing – review & editing. **Sophie Opfergelt:** Conceptualization, Data curation, Funding acquisition, Investigation, Methodology, Resources, Supervision, Validation, Writing – review & editing.

Declaration of competing interest

The authors declare that they have no known competing financial interests or personal relationships that could have appeared to influence the work reported in this paper.

Acknowledgments

The authors would like to thank the entire MOCA platform for their help in acquiring the data necessary to produce this manuscript as well as S. Natali and J. Ledman from Northern Arizona University for the CiPHER setup and the collection of the foliar samples utilized in this study. This work was supported by BELSPO (IMPULS, RT/23/LIFTHAW), by the European Research Council (ERC) under the European Union's Horizon 2020 research and innovation programme (ERC Starting Grant, WeThaw, grant agreement n°714617), by the Fonds National de la Recherche Scientifique (FNRS, FC69480 and CDRMOIST), and by CircleU (Seed Funding CEDRIC).

Appendix A. Supplementary data

Supplementary data to this article can be found online at https://doi.org/10.1016/j.apgeochem.2026.106914.

Data availability

Data will be made available on request.

References

Aciego, S.M., Bourdon, B., Lupker, M., Rickli, J., 2009. A new procedure for separating and measuring radiogenic isotopes (U, Th, Pa, Ra, Sr, Nd, Hf) in ice cores. Chem. Geol. 266 (3–4), 194–204. https://doi.org/10.1016/J.CHEMGEO.2009.06.003.

Aerts, R., 2006. The freezer defrosting: global warming and litter decomposition rates in cold biomes. J. Ecol. 94 (4), 713–724. https://doi.org/10.1111/J.1365-2745.2006.01142.X.

Aerts, R., 2008. Nitrogen supply effects on leaf dynamics and nutrient input into the soil of plant species in a sub-arctic tundra ecosystem. Polar Biol. 32 (2), 207–214. https://doi.org/10.1007/s00300-008-0521-1, 2008 32:2.

Blum, J.D., Erel, Y., 1997. RbSr isotope systematics of a granitic soil chronosequence: the importance of biotite weathering. Geochem. Cosmochim. Acta 61 (15), 3193–3204. https://doi.org/10.1016/S0016-7037(97)00148-8.

Blume-Werry, G., 2021. The belowground growing season. Nature Climate Change 2021 12 (1), 11–12. https://doi.org/10.1038/s41558-021-01243-y, 12(1).

Blume-Werry, G., Milbau, A., Teuber, L.M., Johansson, M., Dorrepaal, E., 2019. Dwelling in the deep – strongly increased root growth and rooting depth enhance plant interactions with thawing permafrost soil. New Phytol. 223 (3), 1328–1339. https://doi.org/10.1111/NPH.15903.

Capo, R.C., Stewart, B.W., Chadwick, O.A., 1998. Strontium isotopes as tracers of ecosystem processes: theory and methods. Geoderma 82 (1–3), 197–225. http://www.scopus.com/inward/record.url?eid=2-s2.0-0031943786&partnerID=40&md5=c202db5b21143f5b4f87bba15f159518.

Chadwick, O.A., Derry, L.A., Vitousek, P.M., Huebert, B.J., Hedin, L.O., 1999. Changing sources of nutrients during four million years of ecosystem development. Nature 397 (6719), 491–497. https://doi.org/10.1038/17276.

Chapin, F.S., Shaver, G.R., Giblin, A.E., Nadelhoffer, K.J., Laundre, J.A., 1995. Responses of arctic tundra to experimental and observed changes in climate. Ecology 76 (3), 694–711. https://doi.org/10.2307/1939337.

Chapin, F.S.C., van Cleve, K., Chapin, M.C., 1979. Soil temperature and nutrient cycling in the tussock growth form of Eriophorum vaginatum. J. Ecol. 67 (1), 169. https://doi.org/10.2307/2259343.

Cornelissen, J.H.C., Van Bodegom, P.M., Aerts, R., Callaghan, T.V., Van Logtestijn, R.S. P., Alatalo, J., Stuart Chapin, F., Gerdol, R., Gudmundsson, J., Gwynn-Jones, D., Hartley, A.E., Hik, D.S., Hofgaard, A., Jónsdóttir, I.S., Karlsson, S., Klein, J.A., Laundre, J., Magnusson, B., Michelsen, A., et al., 2007. Global negative vegetation feedback to climate warming responses of leaf litter decomposition rates in cold biomes. Ecol. Lett. 10 (7), 619–627. https://doi.org/10.1111/J.1461-0248.2007.01051.X.

De Vrese, P., Georgievski, G., Gonzalez Rouco, J.F., Notz, D., Stacke, T., Steinert, N.J., Wilkenskjeld, S., Brovkin, V., 2023. Representation of soil hydrology in permafrost regions may explain large part of inter-model spread in simulated Arctic and subarctic climate. Cryosphere 17 (5), 2095–2118. https://doi.org/10.5194/TC-17-2095-2023.

Deane-Coe, K.K., Mauritz, M., Celis, G., Salmon, V., Crummer, K.G., Natali, S.M., Schuur, E.A.G., 2015. Experimental warming alters productivity and isotopic signatures of tundra mosses. Ecosystems 18 (6), 1070–1082. https://doi.org/10.1007/S10021-015-9884-7.

Demarco, J., Mack, M.C., Syndonia Bret-harte, M., 2014. Effects of arctic shrub expansion on biophysical vs. biogeochemical drivers of litter decomposition. Ecology 95 (7), 1861–1875. http://ecosystems.mbl.edu/ARC.

Drouet, T., Herbauts, J., Gruber, W., Demaiffe, D., 2005. Strontium isotope composition as a tracer of calcium sources in two forest ecosystems in Belgium. Geoderma 126 (3–4), 203–223. https://doi.org/10.1016/j.geoderma.2004.09.010.

Drouet, T., Herbauts, J., Gruber, W., Demaiffe, D., 2007. Natural strontium isotope composition as a tracer of weathering patterns and of exchangeable calcium sources in acid leached soils developed on loess of central Belgium. Eur. J. Soil Sci. 58 (1), 302–319. https://doi.org/10.1111/J.1365-2389.2006.00840.X.

Elmendorf, S.C., Henry, G.H.R., Hollister, R.D., Björk, R.G., Boulanger-Lapointe, N., Cooper, E.J., Cornelissen, J.H.C., Day, T.A., Dorrepaal, E., Elumeeva, T.G., Gill, M., Gould, W.A., Harte, J., Hik, D.S., Hofgaard, A., Johnson, D.R., Johnstone, J.F., Jónsdóttir, I.S., Jorgenson, J.C., et al., 2012. Plot-scale evidence of tundra vegetation change and links to recent summer warming. Nature Climate Change 2012 2 (6), 453–457. https://doi.org/10.1038/nclimate1465, 2(6).

Euskirchen, E.S., McGuire, A.D., Kicklighter, D.W., Zhuang, Q., Clein, J.S., Dargaville, R. J., Dye, D.G., Kimball, J.S., McDonald, K.C., Melillo, J.M., Romanovsky, V.E., Smith, N.V., 2006. Importance of recent shifts in soil thermal dynamics on growing season length, productivity, and carbon sequestration in terrestrial high-latitude ecosystems. Glob. Change Biol. 12 (4), 731–750. https://doi.org/10.1111/J.1365-2486.2006.01113.X.

French, H.M., 2007. Permafrost. The Periglacial Environment 83–115. https://doi.org/10.1002/9781118684931.CH5.

Frost, G.V., Bhatt, U.S., Epstein, H.E., Myers-Smith, I., Phoenix, G.K., Berner, L.T., Bjerke, J.W., Forbes, B.C., Goetz, S.J., Kerby, J.T., Macander, M.J., Park, T., Raynolds, M.K., Tømmervik, H., Walker, D.A., 2020. Arctic Report Card 2020: Tundra Greenness. https://doi.org/10.25923/46RM-0W23.

Gao, S., Song, Y., Song, C., Wang, X., Ma, X., Gao, J., Cheng, X., Du, Y., 2022. Effects of temperature increase and nitrogen addition on the early litter decomposition in permafrost peatlands. Catena 209, 105801. https://doi.org/10.1016/j.catena.2021.105801.

Heijmans, M.M.P.D., Magnússon, R., Lara, M.J., Frost, G.V., Myers-Smith, I.H., van Huissteden, J., Jorgenson, M.T., Fedorov, A.N., Epstein, H.E., Lawrence, D.M., Limpens, J., 2022. Tundra vegetation change and impacts on permafrost. Nat. Rev. Earth Environ. 3 (1), 68–84. https://doi.org/10.1038/S43017-021-00233-0.

Herndon, E., Kinsman-Costello, L., Godsey, S., 2020. Biogeochemical cycling of redox-sensitive elements in Permafrost-Affected ecosystems. Biogeochemical Cycles: Ecological Drivers and Environmental Impact 245–265. https://doi.org/10.1002/9781119413332.CH12.

Hewitt, R.E., Taylor, D.L., Genet, H., McGuire, A.D., Mack, M.C., 2019. Below-ground plant traits influence tundra plant acquisition of newly thawed permafrost nitrogen. J. Ecol. 107 (2), 950–962. https://doi.org/10.1111/1365-2745.13062.

Hicks Pries, C.E., Schuur, E.A.G., Vogel, J.G., Natali, S.M., 2013. Moisture drives surface decomposition in thawing tundra. J. Geophys. Res. Biogeosci. 118, 1133–1143. https://doi.org/10.1002/jgrg.20089.

Hirst, C., Mauclet, E., Monhonval, A., Tihon, E., Ledman, J., Schuur, E.A.G., Opfergelt, S., 2022. Seasonal changes in hydrology and permafrost Degradation Control Mineral element-bound DOC transport from permafrost soils to streams. Glob. Biogeochem. Cycles 36 (2). https://doi.org/10.1029/2021GB007105.

Hobbie, S.E., 1996. Temperature and plant species control over litter decomposition in Alaskan tundra. Ecol. Monogr. 66 (4), 503–522. https://doi.org/10.2307/2963492.

Hossain, M.F., Chen, W., Zhang, Y., 2015. Bulk density of mineral and organic soils in the Canada's Arctic and sub-Arctic. Inf. Process. Agric. 2 (3–4), 183–190. https://doi.org/10.1016/j.inpa.2015.09.001.

Iversen, C.M., Sloan, V.L., Sullivan, P.F., Euskirchen, E.S., Mcguire, A.D., Norby, R.J., Walker, A.P., Warren, J.M., Wullschleger, S.D., 2015. The unseen iceberg: plant roots in arctic tundra. New Phytol. 205 (1), 34–58. https://doi.org/10.1111/NPH.13003.

Jónsdóttir, I.S., Magnússon, B., Gudmundsson, J., Elmarsdóttir, Á., Hjartarson, H., 2005. Variable sensitivity of plant communities in Iceland to experimental warming. Glob. Change Biol. 11 (4), 553–563. https://doi.org/10.1111/J.1365-2486.2005.00928.X.

Jobbágy, E.G., Jackson, R.B., 2004. The uplift of soil nutrients by plants: biogeochemical consequences across scales. Ecology 85 (9), 2380–2389.

Jonasson, S., Stuart Chapin, F., 1985. Significance of sequential leaf development for nutrient balance of the cotton sedge, Eriophorum vaginatum L. Oecologia 67 (4), 511–518. https://doi.org/10.1007/BF00790022.

Jonasson, S., Stuart Chapin, F., 1991. Seasonal uptake and allocation of phosphorus in Eriophorum vaginatum L measured by labelling with 32P. New Phytol. 118 (2), 349–357. https://doi.org/10.1111/j.1469-8137.1991.tb00987.x.

Jorgenson, J.C., Raynolds, M.K., Reynolds, J.H., Benson, A.M., 2015. Twenty-Five year record of changes in plant cover on tundra of Northeastern Alaska. Arctic Antarct. Alpine Res. 47 (4), 785–806. https://doi.org/10.1657/AAAR0014-097.

Jorgenson, M.T., Racine, C.H., Walters, J.C., Osterkamp, T.E., 2001. Permafrost degradation and ecological changes associated with a warming climate in central Alaska. Clim. Change 48 (4), 551–579. https://doi.org/10.1023/A:1005667424292.

Jorgenson, M.T., Shur, Y.L., Pullman, E.R., 2006. Abrupt increase in permafrost degradation in Arctic Alaska. Geophys. Res. Lett. 33 (2). https://doi.org/10.1029/2005GL024960.

Kadej, Stephanie, Taylor, Meghan, Salmon, Verity, Natali, Susan, Mauritz, Marguerite, Pegoraro, Elaine, Schuur, Edward, 2022. Eight mile Lake research watershed. Carbon in Permafrost Experimental Heating Research (Cipehr): Aboveground Plant Biomass, 2009-2017, 2021. Bonanza Creek LTER - University of Alaska Fairbanks. BNZ, p. 501. https://doi.org/10.6073/pasta/bbc20b124e75f1484ea7ebdda0462c30. http://www.lter.uaf.edu/data/data-detail/id/501.

Karlsson, P.S., 1992. Leaf longevity in evergreen shrubs: variation within and among European species. Oecologia 91 (3), 346–349. https://doi.org/10.1007/BF00317622/METRICS.

Keuper, F., Dorrepaal, E., van Bodegom, P.M., van Logtestijn, R., Venhuizen, G., van Hal, J., Aerts, R., 2017. Experimentally increased nutrient availability at the permafrost thaw front selectively enhances biomass production of deep-rooting subarctic peatland species. Glob. Change Biol. 23 (10), 4257–4266. https://doi.org/10.1111/GCB.13804.

Keuper, F., van Bodegom, P.M., Dorrepaal, E., Weedon, J.T., van Hal, J., van Logtestijn, R.S.P., Aerts, R., 2012. A frozen feast: thawing permafrost increases plant-available nitrogen in subarctic peatlands. Glob. Change Biol. 18 (6), 1998–2007. https://doi.org/10.1111/J.1365-2486.2012.02663.X.

Koch, J.C., Runkel, R.L., Striegl, R., McKnight, D.M., 2013. Hydrologic controls on the transport and cycling of carbon and nitrogen in a boreal catchment underlain by continuous permafrost. J. Geophys. Res. Biogeosci. 118 (2), 698–712. https://doi.org/10.1002/JGRG.20058.

Letts, M.G., Comer, N.T., Roulet, N.T., Skarupa, M.R., Verseghy, D.L., 2000. Parametrization of peatland hydraulic properties for the Canadian land surface scheme. Atmos.-Ocean 38 (1), 141–160. https://doi.org/10.1080/07055900.2000.9649643.

Mauclet, E., Agnan, Y., Hirst, C., Monhonval, A., Pereira, B., Vandeuren, A., Villani, M., Ledman, J., Taylor, M., Jasinski, B.L., Schuur, E.A.G., Opfergelt, S., 2022. Changing sub-Arctic tundra vegetation upon permafrost degradation: impact on foliar mineral element cycling. Biogeosciences 19 (9), 2333–2351. https://doi.org/10.5194/BG-19-2333-2022.

Mauclet, E., Hirst, C., Monhonval, A., Stevenson, E.I., Gérard, M., Villani, M., Dailly, H., Schuur, E.A.G., Opfergelt, S., 2023a. Tracing changes in base cation sources for Arctic tundra vegetation upon permafrost thaw. Geoderma 429, 116277. https://doi.org/10.1016/J.GEODERMA.2022.116277.

Mauclet, E., Villani, M., Monhonval, A., Hirst, C., Schuur, E.A.G., Opfergelt, S., 2023b. Quantifying exchangeable base cations in permafrost: a reserve of nutrients about to thaw. Earth Syst. Sci. Data 15 (9), 3891–3904. https://doi.org/10.5194/ESSD-15-3891-2023.

Mauritz, M., Bracho, R., Celis, G., Hutchings, J., Natali, S.M., Pegoraro, E., Salmon, V.G., Schädel, C., Webb, E.E., Schuur, E.A.G., 2017. Nonlinear CO2 flux response to 7 years of experimentally induced permafrost thaw. Glob. Change Biol. 23 (9), 3646–3666. https://doi.org/10.1111/GCB.13661.

McCrystall, M.R., Stroeve, J., Serreze, M., Forbes, B.C., Screen, J.A., 2021. New climate models reveal faster and larger increases in Arctic precipitation than previously projected. Nat. Commun. 12 (1), 1–12. https://doi.org/10.1038/s41467-021-27031-y, 2021 12:1.

Mcguire, A.D., Anderson, L.G., Christensen, T.R., Scott, D., Laodong, G., Hayes, D.J., Martin, H., Lorenson, T.D., Macdonald, R.W., Nigel, R., 2009. Sensitivity of the carbon cycle in the Arctic to climate change. Ecol. Monogr. 79 (4), 523–555. https://doi.org/10.1890/08-2025.1.

McLaren, J.R., Buckeridge, K.M., van de Weg, M.J., Shaver, G.R., Schimel, J.P., Gough, L., 2017. Shrub encroachment in Arctic tundra: betula nana effects on above- and belowground litter decomposition. Ecology 98 (5), 1361–1376. https://doi.org/10.1002/ECY.1790.

Monhonval, A., Hirst, C., Strauss, J., Schuur, E.A.G., Opfergelt, S., 2023. Strontium isotopes trace the dissolution and precipitation of mineral organic carbon interactions in thawing permafrost. Geoderma 433, 116456. https://doi.org/10.1016/J.GEODERMA.2023.116456.

Monhonval, A., Mauclet, E., Pereira, B., Vandeuren, A., Strauss, J., Grosse, G., Schirrmeister, L., Fuchs, M., Kuhry, P., Opfergelt, S., 2021. Mineral element stocks in the yedoma domain: a novel method applied to ice-rich permafrost regions. Front. Earth Sci. 9, 703304. https://doi.org/10.3389/FEART.2021.703304/BIBTEX.

Moore, T.R., Dalva, M., 1993. The influence of temperature and water table position on carbon dioxide and methane emissions from laboratory columns of peatland soils. J. Soil Sci. 44 (4), 651–664. https://doi.org/10.1111/j.1365-2389.1993.tb02330.x.

Myers-Smith, I.H., Elmendorf, S.C., Beck, P.S.A., Wilmking, M., Hallinger, M., Blok, D., Tape, K.D., Rayback, S.A., Macias-Fauria, M., Forbes, B.C., Speed, J.D.M., Boulanger-Lapointe, N., Rixen, C., Lévesque, E., Schmidt, N.M., Baittinger, C., Trant, A.J., Hermanutz, L., Collier, L.S., et al., 2015. Climate sensitivity of shrub growth across the tundra biome. Nat. Clim. Change 5 (9), 887–891. https://doi.org/10.1038/nclimate2697, 2015 5:9.

Myers-Smith, I.H., Kerby, J.T., Phoenix, G.K., Bjerke, J.W., Epstein, H.E., Assmann, J.J., John, C., Andreu-Hayles, L., Angers-Blondin, S., Beck, P.S.A., Berner, L.T., Bhatt, U. S., Bjorkman, A.D., Blok, D., Bryn, A., Christiansen, C.T., Cornelissen, J.H.C., Cunliffe, A.M., Elmendorf, S.C., et al., 2020. Complexity revealed in the greening of the Arctic. Nature Climate Change 2020 10 (2), 106–117. https://doi.org/10.1038/s41558-019-0688-1, 10(2).

Nadelhoffer, K.J., Giblin, A.E., Shaver, G.R., Laundre, J.A., 1991. Effects of temperature and substrate quality on element mineralization in six arctic soils. Ecology 72 (1), 242–253. https://doi.org/10.2307/1938918.

Natali, S.M., Schuur, E.A.G., Rubin, R.L., 2012. Increased plant productivity in Alaskan tundra as a result of experimental warming of soil and permafrost. J. Ecol. 100 (2), 488–498. https://doi.org/10.1111/J.1365-2745.2011.01925.X.

Natali, S.M., Schuur, E.A.G., Trucco, C., Hicks Pries, C.E., Crummer, K.G., Baron Lopez, A.F., 2011. Effects of experimental warming of air, soil and permafrost on carbon balance in Alaskan tundra. Glob. Change Biol. 17 (3), 1394–1407. https://doi.org/10.1111/J.1365-2486.2010.02303.X.

Opfergelt, Sophie, Hirst, Catherine, Schuur, Edward, Mauclet, Elisabeth, Monhonval, Arthur, Ledman, Justin, 2021. Eight Mile Lake Research Watershed, Thaw Gradient: geochemistry of soil pore waters sampled in May 2018 (0 - 20 Cm depth) and August 2019 (0-120 Cm depth) at Gradient site, 2018-2019. BNZ 780. https://doi.org/10.6073/pasta/f3b2f5aa791f8df5f7bae640f079296b. Bonanza Creek LTER - University of Alaska Fairbanks. http://www.lter.uaf.edu/data/data-detail/id/780.

Osterkamp, T.E., Jorgenson, M.T., Schuur, E.A.G., Shur, Y.L., Kanevskiy, M.Z., Vogel, J. G., Tumskoy, V.E., 2009. Physical and ecological changes associated with warming permafrost and thermokarst in Interior Alaska. Permafr. Periglac. Process. 20 (3), 235–256. https://doi.org/10.1002/PPP.656.

Peng, X., Zhang, T., Frauenfeld, O.W., Mu, C., Wang, K., Wu, X., Guo, D., Luo, J., Hjort, J., Aalto, J., Karjalainen, O., Luoto, M., 2023. Active layer thickness and permafrost area projections for the 21st century. Earths Future 11 (8). https://doi.org/10.1029/2023EF003573 e2023EF003573.

Pries, C.E.H., Schuur, E.A.G., Crummer, K.G., 2012. Holocene carbon stocks and carbon accumulation rates altered in soils undergoing permafrost thaw. Ecosystems 15 (1), 162–173. https://doi.org/10.1007/S10021-011-9500-4.

Ravansari, R., Wilson, S.C., Tighe, M., 2020. Portable X-ray fluorescence for environmental assessment of soils: not just a point and shoot method. Environ. Int. 134. https://doi.org/10.1016/J.ENVINT.2019.105250.

Ravansari, R., Lemke, L.D., 2018. Portable X-ray fluorescence trace metal measurement in organic rich soils: pXRF response as a function of organic matter fraction. Geoderma 319, 175–184. https://doi.org/10.1016/J.GEODERMA.2018.01.011.

Reynolds, A.C., Quade, J., Betancourt, J.L., 2012. Strontium isotopes and nutrient sourcing in a semi-arid woodland. Geoderma 189–190, 574–584. https://doi.org/10.1016/J.GEODERMA.2012.06.029.

Rodenhizer, H., Ledman, J., Mauritz, M., Natali, S.M., Pegoraro, E., Plaza, C., Romano, E., Schädel, C., Taylor, M., Schuur, E., 2020. Carbon thaw rate doubles when accounting for subsidence in a permafrost warming experiment. J. Geophys. Res. Biogeosci. 125 (6). https://doi.org/10.1029/2019JG005528 e2019JG005528.

Salmon, V.G., Soucy, P., Mauritz, M., Celis, G., Natali, S.M., Mack, M.C., Schuur, E.A.G., 2016. Nitrogen availability increases in a tundra ecosystem during five years of experimental permafrost thaw. Glob. Change Biol. 22 (5), 1927–1941. https://doi.org/10.1111/GCB.13204.

Schuur, E.A.G., Bracho, R., Celis, G., Belshe, E.F., Ebert, C., Ledman, J., Mauritz, M., Pegoraro, E.F., Plaza, C., Rodenhizer, H., Romanovsky, V., Schädel, C., Schirokauer, D., Taylor, M., Vogel, J.G., Webb, E.E., 2021. Tundra underlain by thawing Permafrost persistently emits carbon to the atmosphere over 15 years of measurements. J. Geophys. Res. Biogeosci. 126 (6). https://doi.org/10.1029/2020JG006044 e2020JG006044.

Schuur, E.A.G., Crummer, K.G., Vogel, J.G., MacK, M.C., 2007. Plant species composition and productivity following permafrost thaw and thermokarst in Alaskan tundra. Ecosystems 10 (2), 280–292. https://doi.org/10.1007/S10021-007-9024-0.

Schuur, E.A.G., Hicks Pries, C., Mauritz, M., Pegoraro, E., Rodenhizer, H., See, C., Ebert, C., 2023. Ecosystem and Soil Respiration Radiocarbon Detects Old Carbon Release as a Fingerprint of Warming and Permafrost Destabilization with Climate Change. Philos. Trans. A Math. Phys. Eng. Sci. 381 (2261), 20220201. https://doi.org/10.1098/rsta.2022.0201, 2023.

Schuur, E.A.G., MacK, M.C., 2018. Ecological response to permafrost thaw and consequences for local and global ecosystem services. Annu. Rev. Ecol. Evol. Syst. 49, 279–301. https://doi.org/10.1146/ANNUREV-ECOLSYS-121415-032349.

Shaver, G.R., Giblin, A.E., Nadelhoffer, K.J., Thieler, K.K., Downs, M.R., Laundre, J.A., Rastetter, E.B., 2006. Carbon turnover in Alaskan tundra soils: effects of organic matter quality, temperature, moisture and fertilizer. J. Ecol. 94 (4), 740–753. https://doi.org/10.1111/J.1365-2745.2006.01139.X.

Shaver, G.R., Syndonia Bret-Harte, M., Jones, M.H., Johnstone, J., Gough, L., Laundre, J., Chapin, F.S., 2001. Species composition interacts with fertilizer to control long-term

change in tundra productivity. Ecology 82 (11), 3163–3181. https://doi.org/10.1890/0012-9658.
Shaver, G.R., Chapin, F.S., 1991. Production: biomass relationships and element cycling in contrasting arctic vegetation types. Ecol. Monogr. 61 (1), 1–23. https://doi.org/10.2307/1942997.
Song, Y., Song, C., Ren, J., Tan, W., Jin, S., Jiang, L., 2018. Influence of nitrogen additions on litter decomposition, nutrient dynamics, and enzymatic activity of two plant species in a peatland in Northeast China. Sci. Total Environ. 625, 640–646. https://doi.org/10.1016/j.scitotenv.2017.12.311.
Sturm, M., Racine, C., Tape, K., 2001. Increasing shrub abundance in the Arctic. Nature 411 (6837), 546–547. https://doi.org/10.1038/35079180.
Van Der Kolk, H.J., Heijmans, M.M.P.D., Van Huissteden, J., Pullens, J.W.M., Berendse, F., 2016. Potential Arctic tundra vegetation shifts in response to changing temperature, precipitation and permafrost thaw. Biogeosciences 13 (22), 6229–6245. https://doi.org/10.5194/BG-13-6229-2016.
Villani, M., Mauclet, E., Agnan, Y., Druel, A., Jasinski, B., Taylor, M., Schuur, E.A.G., Opfergelt, S., 2022. Mineral element recycling in topsoil following permafrost degradation and a vegetation shift in sub-Arctic tundra. Geoderma 421. https://doi.org/10.1016/J.GEODERMA.2022.115915.
Vitousek, P.M., Kennedy, M.J., Derry, L.A., Chadwick, O.A., 1999. Weathering versus atmospheric sources of strontium in ecosystems on young volcanic soils. Oecologia 121 (2), 255–259. https://doi.org/10.1007/S004420050927.
Vogel, J., Schuur, E.A.G., Trucco, C., Lee, H., 2009. Response of CO2 exchange in a tussock tundra ecosystem to permafrost thaw and thermokarst development. J. Geophys. Res. Biogeosci. 114 (4). https://doi.org/10.1029/2008JG000901.
Walvoord, M.A., Kurylyk, B.L., 2016. Hydrologic impacts of thawing Permafrost—A review. Vadose Zone J. 15 (6), 1–20. https://doi.org/10.2136/VZJ2016.01.0010/315784.
Wang, P., Limpens, J., Mommer, L., van Ruijven, J., Nauta, A.L., Berendse, F., Schaepman-Strub, G., Blok, D., Maximov, T.C., Heijmans, M.M.P.D., 2017. Above- and below-ground responses of four tundra plant functional types to deep soil heating and surface soil fertilization. J. Ecol. 105 (4), 947–957. https://doi.org/10.1111/1365-2745.12718.
Wang, X., Tang, Z., 2020. The first large-scale bioavailable Sr isotope map of China and its implication for provenance studies. Earth Sci. Rev. 210, 103353. https://doi.org/10.1016/J.EARSCIREV.2020.103353.
Warren, Julia A., McGroarty, Megan, Schaedel, Christina, Rodenhizer, Heidi G., Mauritz, Marguerite, Taylor, Meghan, Ledman, Justin, Natali, Susan, Schuur, Edward, 2025. Eight Mile Lake Research Watershed, Carbon in Permafrost Experimental Heating Research (Cipehr): Seasonal Water Table Depth Data, 2012-2025. Bonanza Creek LTER - University of Alaska Fairbanks. BNZ. https://doi.org/10.6073/pasta/3ae80c218ef33b64117efad8e24fc127, 554. http://www.lter.uaf.edu/data/data-detail/id/554.
White, P.J., 2001. The pathways of calcium movement to the xylem. J. Exp. Bot. 52 (358), 891–899. https://doi.org/10.1093/jexbot/52.358.891.